IKF91 – 1

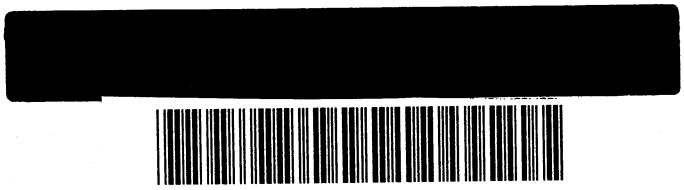

Study of the Energy Flow in Sulphur– and Oxygen–Nucleus Collisions at 60 and 200 GeV/Nucleon.

NA35 Collaboration

INSTITUT FÜR KERNPHYSIK

Johann Wolfgang Goethe – Universität

Frankfurt am Main

August–Euler–Strasse 6

D–6000 Frankfurt am Main 90

Study of the Energy Flow in Sulphur– and Oxygen–Nucleus Collisions at 60 and 200 GeV/Nucleon.

NA35 Collaboration

ABSTRACT

We report on a systematic study of midrapidity transverse energy production and forward energy flow in interactions of ^{16}O and ^{32}S projectiles with S, Cu, Ag and Au targets at 60 and 200 GeV/nucleon. The variation of the shape of the E_T distributions with target and projectile mass can be understood from collision geometry. Average E_T values determined for central collisions show an increasing stopping power for heavier target nuclei. A higher relative stopping is observed at 60 GeV/nucleon than at 200 GeV/nucleon. Bjorken estimates of the energy density reach approximately 3 GeV/fm^3 in high E_T events at 200 GeV/nucleon with ^{16}O and ^{32}S projectiles. The systematics of the data and the shapes of E_T and pseudorapidity distributions are well described by the Lund model Fritiof.

(Submitted to Zeitschrift für Physic C)

NA35-Collaboration

J. Bächler[8], J. Bartke[5], H. Bialkowska[12], R. Bock[6], R. Brockmann[6], P. Buncic[13], S.I. Chase[3], I. Derado[10], V. Eckardt[10], J. Eschke[7], C. Favuzzi[2], D. Ferenc[13], B. Fleischmann[6], P. Foka[6], M. Fuchs[6], M. Gazdzicki[11], H.J. Gebauer[10], E. Gladysz[5], C. Guerra[6], J.W. Harris[3], W. Heck[7], M. Hoffmann[8], T. Humanic[6,a], S. Kabana[7], K. Kadija[13], A. Karabarbounis[1], R. Keidel[9], J. Kosiec[7], M. Kowalski[10], A. Kühmichel[7], M. Lahanas[7], J.Y. Lee[7], M. LeVine[7,14], A. Ljubicic Jr.[13], S. Margetis[7], E. Nappi[2], G. Odyniec[3], G. Paic[6,13], A.D. Panagiotou[1], A. Petridis[1], J. Pfennig[4], A. Piper[9], F. Posa[2], H.G. Pugh[3], F. Pühlhofer[9], G. Rai[3], W. Rauch[10], R. Renfordt[7], D. Röhrich[7], G. Roland[7], H. Rothard[7], K. Runge[8], A. Sandoval[6], E. Schmidt[7], N. Schmitz[10], E. Schmoetten[8], I. Schneider[7], L.S. Schroeder[3], P. Seyboth[10], J. Seyerlein[10], E. Skrzypczak[11], P. Spinelli[2], R. Stock[7], H. Ströbele[7], L. Teitelbaum[3], A. Thomas[7], S. Tonse[3], G. Vasileiadis[1], G. Vesztergombi[10,b], D. Vranic[13], S. Wenig[7]

[1]Department of Physics, University of Athens, Athens, Greece
[2]Dipartimento di Fisica, Università di Bari and INFN Bari, Bari, Italy
[3]Lawrence Berkeley Laboratory, Berkeley, CA, USA
[4]CERN, Geneva, Switzerland
[5]Institute of Nuclear Physics, Cracow, Poland
[6]Gesellschaft für Schwerionenforschung (GSI), Darmstadt, Federal Republic of Germany
[7]Fachbereich Physik der Universität, Frankfurt, Federal Republic of Germany
[8]Fakultät für Physik der Universität, Freiburg, Federal Republic of Germany
[9]Fachbereich Physik der Universität, Marburg, Federal Republic of Germany
[10]Max–Planck–Institut für Physik und Astrophysik, München,
Federal Republic of Germany
[11]Institute for Experimental Physics, University of Warsaw, Warsaw, Poland
[12]Institute for Nuclear Studies, Warsaw, Poland
[13]Rudjer Boskovic Institute, Zagreb, Yugoslavia
[14]Department of Physics, Brookhaven National Laboratory, Upton, NY, USA

[a]Now at Physics Dept., University of Pittsburg, USA
[b]On leave from Central Research Institute of Physics, Budapest, Hungary

1 Introduction

The production of transverse energy (E_T) in high energy nucleus–nucleus collisions results from degradation of the initial longitudinal energy of the participating nucleons, which occurs during interpenetration of the target/projectile nuclei, and is expected to lead to a short–lived state of high energy density. Both the energy density (ε) and reaction volume (V) may significantly exceed levels characteristic of hadron–hadron collisions where $\varepsilon \approx 1$ GeV/fm^3 and V is a few fm^3. This has led to speculation concerning the possible formation of a Quark Gluon Plasma (QGP), i.e. a deconfined state of quarks and gluons [1]. A necessary condition for QGP formation is high energy densities, $\varepsilon \approx 3$ GeV/fm^3. Initial calorimetric studies have shown that these conditions are created in high E_T, i.e. central collision, events of ^{16}O and ^{32}S projectiles with heavy nuclei at projectile energies of 200 GeV/nucleon [2]. Furthermore, the nuclear stopping power in these events significantly exceeds the level observed in nucleon–nucleon collisions at the same center–of–mass (c.m.) energy [2], [3]. The definition of stopping power varies in the literature. A common approach to determining the stopping power is to measure the fraction of the available energy $\sqrt{s}$ that is shifted away from target and projectile rapidity to a region of about $|\Delta y| \approx 1$ centered at midrapidity. Unlike in hadron–hadron collisions the numbers of projectile and target participants in a nucleus–nucleus collision must be specified in order to define the kinematics of the collision. Two different approaches may be taken:

1. Distributions in transverse momentum (p_T) and rapidity (y) of participating nucleons in the final state can be measured by identification of the distributions of net–baryon number. This is a task for charged–particle exclusive analysis in 4π acceptance. A study to determine the 'stopped' fraction of the c.m. energy by measuring the net–baryon p_T, y distributions was carried out by studying central S + S collisions [4] with the NA35 streamer chamber. The total energy loss of participating baryons manifests itself in the energy contained in created particles. The distribution of this energy in momentum space is reflected in the p_T, y distributions of identified hadrons. The nuclear stopping power may thus be determined from the ratio of the total energy lost by the incident nucleons to the total c.m. energy.

2. Alternatively, one can measure via calorimetric study the total transverse energy created in a central collision and its distribution in pseudorapidity. The participating baryons cannot be identified separately in this case. Therefore, in order to determine the average number of projectile/target nucleons participating in the nucleus–nucleus collisions, a geometrical model is employed. This procedure establishes the kinematic variables. The nuclear stopping power is determined by comparing the observed total transverse energy to the total available c.m. energy obtained from the model.

In the present study we have adopted the second approach. A systematic measurement of

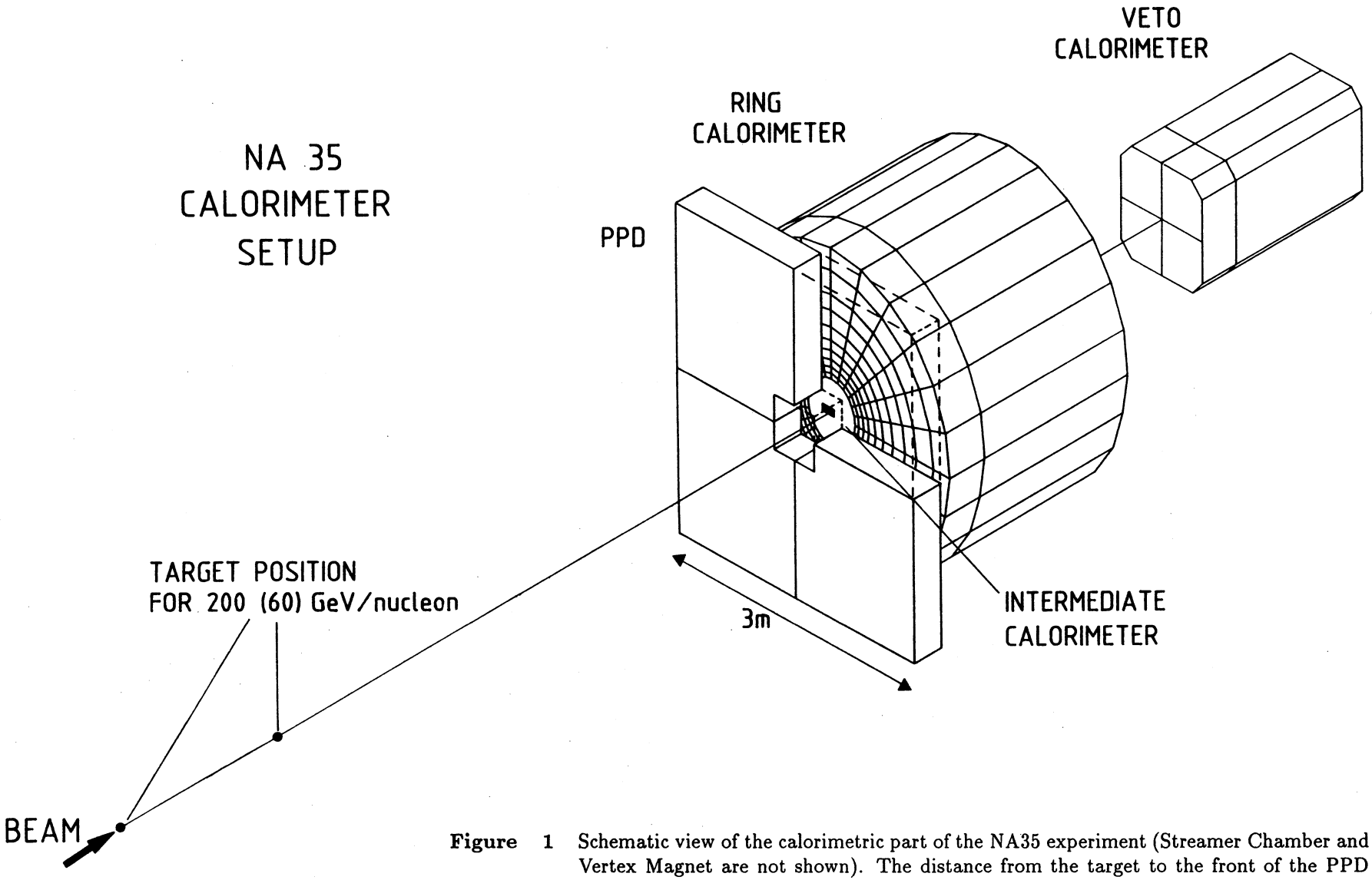

Figure 1 Schematic view of the calorimetric part of the NA35 experiment (Streamer Chamber and Vertex Magnet are not shown). The distance from the target to the front of the PPD was 5.0 m (6.4 m) for 60 (200) GeV/nucleon.

electromagnetic and hadronic transverse energy distributions as a function of pseudorapidity was undertaken. Interactions induced by 60 and 200 GeV/nucleon ^{16}O, and 200 GeV/nucleon ^{32}S and proton projectiles with various target nuclei were studied using the CERN SPS. We present results on forward energy flow, transverse energy production and correlations between these two observables. Transverse energy distributions as a function of pseudorapidity from peripheral to central collisions were extracted for various projectile/target combinations. We use the Lund Fritiof model [5] for comparision to the data and demonstrate how the impact parameter, and thus the collision centrality, correlates with quantities measured by the calorimeters.

Our conclusions are that the nuclear stopping power increases from 42 percent in ^{32}S + ^{32}S average central collisions to 52 percent in ^{32}S + Au at 200 GeV/nucleon and that high energy densities, of the order of 3 GeV/fm^3, are observed in ^{32}S + heavy target reactions. The Fritiof model reproduces these observations. The mean ratio of electromagnetic to hadronic transverse energy is systematically lower than the corresponding Fritiof predictions, in central collisions.

2 Experimental Setup

The NA35 experiment [6] is well suited for a survey study of ^{16}O and ^{32}S induced reactions on a variety of targets. It consists of a Streamer Chamber in a superconducting Vertex Magnet followed by a set of calorimeters which covers pseudorapidities $\eta > 2$. A perspective view of the calorimeters in the experimental setup, without the Vertex Magnet or Streamer Chamber, is shown in Fig. 1. The beam particles are selected by a 5 mm quartz Cherenkov counter 25 m upstream of the target. This counter has single charge resolution up to ^{32}S. A series of scintillator veto counters downstream, the innermost having a hole of 1 cm diameter, rejects events with halo particles or interactions in the quartz. The beam is again selected with a 300 μm thin scintillator counter, placed close to the target. The targets are placed at the entrance of the Streamer Chamber. A target thickness of about 1% of an interaction length for ^{16}O was used for Au, Ag, Cu, S and Al. At the exit of the Streamer Chamber 4 m downstream from the target, a 3 cm diameter, 1 mm thick scintillator counter is used to provide an interaction trigger by selecting events which produce a pulse height less than that of the projectile. The forward angles are covered by a set of four calorimeters to measure the energy of the reaction products. The angular domain $\vartheta < 0.3^0$, which corresponds to the projectile fragmentation region, is covered by a 'Veto' calorimeter. The next larger angular interval from 0.3^0 – 2.2^0 is covered by a single cell electromagnetic and hadronic Intermediate Calorimeter, with outer diameter 53 cm. The largest angle domain is covered by the Photon Position Detector (PPD), which is an electromagnetic calorimeter of high granularity, consisting of alternating layers of lead and planes of proportional tubes read out by 3072 ADC channels. The PPD is 3 m x 3 m in size and has a depth of 9.8 radiation lengths and 0.5 interaction lengths.

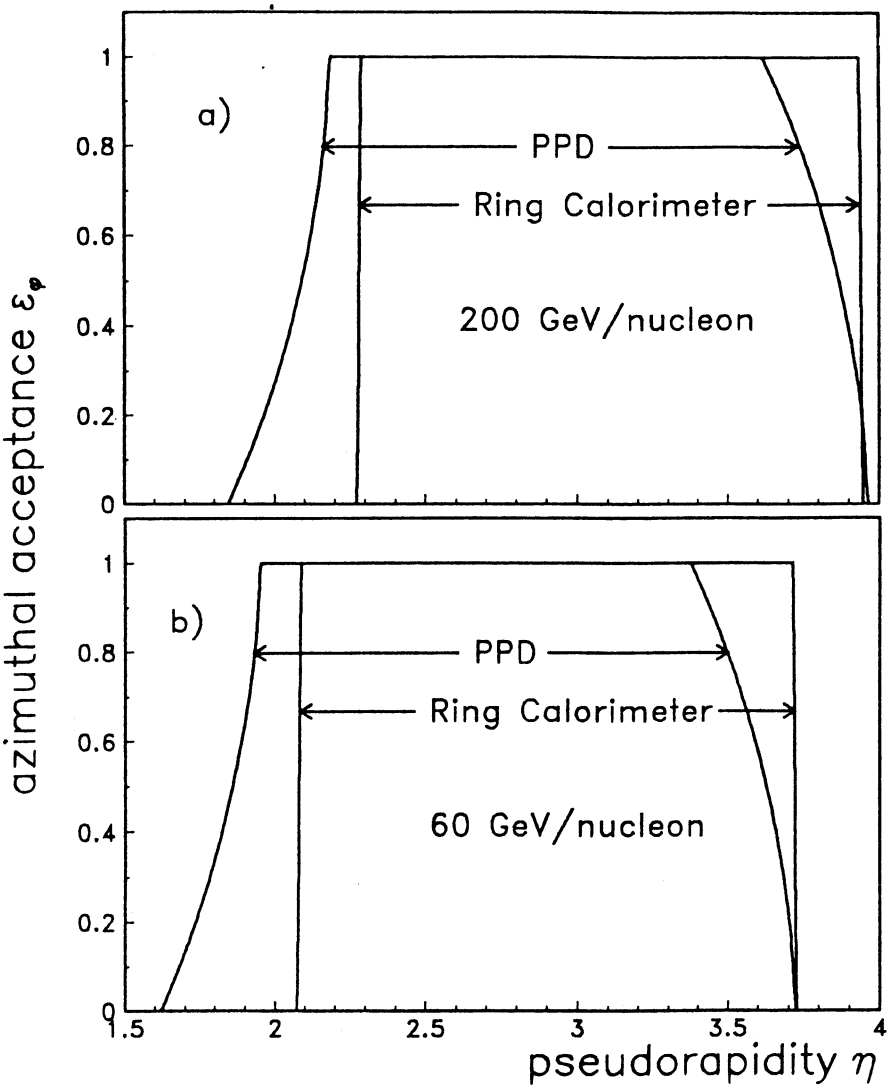

Figure 2 Azimuthal acceptance of the midrapidity calorimeters (PPD and Ring) for 60 and 200 GeV/nucleon. The quadratic shape of the front face of the PPD produces a gradual onset of its acceptance (see Table 1 and compare y_{cm} values given in Table 9).

Acceptances	200 GeV	60 GeV
Ring Calorimeter		
η interval	2.28–3.94	2.08–3.72
$\Delta\eta$	1.66	1.64
$<\eta>$	3.11	2.90
PPD		
η interval with full ϕ coverage	2.18–3.61	1.95–3.37
η interval with partial ϕ coverage	1.85–3.96	1.62–3.72
$\Delta\eta_{eff}$	1.78	1.77
$<\eta>$	2.96	2.73

Table 1 Acceptances of the NA35 midrapidity calorimeters as used for 60 and 200 GeV/nucleon.

It has an inner square hole of 50 cm x 50 cm and is backed by the Ring Calorimeter which has a barrel shape, is 3 m in diameter with an inner hole of 56 cm diameter. The Ring Calorimeter is subdivided into 240 cells, 24 in azimuth and 10 radially with the ring sizes covering equal intervals in pseudorapidity. The PPD and the Ring Calorimeter can be moved together and were positioned to cover the midrapidity region at each incident energy. The acceptances for the PPD and Ring Calorimeter are shown in Fig. 2 and summarized in Table 1.

Three different types of triggers were used in the experiment: an interaction trigger based on the signal of the scintillation counter downstream of the Streamer Chamber, a trigger on the Veto Calorimeter signal which selected events with a forward energy of less than a certain threshold, and a trigger on the E_T seen by the PPD (about 2/3 of its signal is of electromagnetic origin). All triggers were run in each of two configurations: 1) with the field of the Vertex Magnet switched off to preserve the axial symmetry important for the calorimetric study and 2) with a 1.5 T field allowing for charged particle momentum measurements in the Streamer Chamber. In this paper we present the data taken in the field off configuration.

All NA35 calorimeters except the Intermediate Calorimeter have been used in previous experiments (NA5, NA24). Their behaviour and calibration were studied in detail and are published elsewhere [7], [8]. The response to electrons is linear even to energies below 1 GeV. For hadrons the response was studied only down to 10 GeV, which is the lowest hadron energy that the H2 beamline of the CERN SPS can deliver. No calibration was possible at lower energies since neither the entire detector nor its single cells could be transported to another beam line. However, a test of a prototype of the Ring Calorimeter exhibits a linear response to hadrons down to 2 GeV for the peak (but not the mean) of the signal spectrum. Also, calibration data for hadrons at 20 GeV recorded with this prototype were used to determine the effects of inhomogeneities of the Ring Calorimeter (especially near the readout rods), slanting incidence and nonlinear response at low energies. The energy dependence of the energy resolution and the asymmetry of the response spectra were parametrized and were extrapolated down to low energies. The asymmetry has the effect that the mean of the distribution is higher than the peak position. The study of the energy dependence of the asymmetry demonstrated that the ratio mean/peak rises quickly toward low energies and reaches values of about 1.5 at 1 GeV.

The effect on the quality of the Ring Calorimeter simulation of calibrating the prototype data without a PPD in front is negligible. This conclusion is based on the agreement of the prototype spectral shape and asymmetry with the calibration data obtained for the PPD–Ring calorimeter setup at a hadron energy of 10 GeV. From the response simulation we obtain, for each calorimeter ring, an energy–dependent correction factor that includes the effects of response inhomogeneity in the Ring Calorimeter. These factors are consistent with the low energy non–linearity (variation of the e/π ratio) known for calorimeters similar to the Ring calorimeter [9]. The energy–dependent

correction factors were applied to Fritiof–generated events to extract, for every ring, a single factor that corrects on average for realistic particle energy spectra. These factors turned out to be independent of the projectile–target system and the centrality of the collisions and thus could be applied as general corrections. A final overall fine–tuning of the calibration was based on a 10 GeV hadron calibration.

To fully exploit the dynamic range of the ADCs for the energies expected for sulphur as projectile, the photomultiplier voltages were changed between the oxygen and sulphur runs. For sulphur–oxygen comparisons we used as reference p+Au E_T spectra that were taken together with the oxygen and sulphur runs. From these data the PPD and Ring calibrations were adjusted for the two data–taking periods. We adopted this procedure instead of the alternative option to depend on individual calibrations with electrons and hadrons for the separate run periods because the global illumination of the calorimeters in proton–nucleus collisions is more representative of the nucleus–nucleus collision situation than any local calibration with fixed energy hadron beams. This method is limited only by the statistics that could be achieved for the p+Au E_T spectra.

The Ring Calorimeter data were further corrected for variations in the response of individual cells in each ring. The time–consuming procedure of scanning with calibration beams could be dispensed with as nucleus–nucleus collisions illuminate the complete detector so well that we could equalize the cells by their average response assuming symmetry in azimuth.

The e/π ratio was found to be 1.49 for the PPD, and 1.6 for the electromagnetic front part of the Ring. The energy resolution $\sigma(E)/E$ for electromagnetic and hadronic showers in the calorimeter system was found to be $30\%/\sqrt{E}$ and $100\%/\sqrt{E}$, respectively.

3 Data analysis

With the Streamer Chamber situated directly behind the target, material of about 2% of an interaction length for S projectiles is unavoidable in the path of the beam to the interaction scintillator detector. For a minimum bias trigger, this led to a high trigger rate for events whose interaction was not in the target. In order to have a reasonable fraction of target interactions in the recorded data, a target thickness of about 1% of a nucleus–nucleus interaction length was used, which represented a compromise in obtaining a high fraction of target events and, on the other hand, reducing the probability of secondary interactions and e^+e^- pair production in the target.

Runs with proton projectiles on a Au target 4–fold thicker than the normal one did not show a significant difference in the spectra, due to possible secondary interactions, even several orders of magnitude lower in cross section from the peak of the distribution [10]. Therefore, for the observables reported, secondary interactions can be neglected in the calorimeter data. For minimum bias triggers it was essential to record approximately the same number of events for target–in and

target–out. Non–target interactions were subtracted by means of the latter runs. For low E_T events the statistical errors are relatively large due to the background subtraction. To construct the final distributions, up to four different successive trigger thresholds were employed besides the interaction trigger, the harder ones being essentially background free.

The transverse energy, E_T, is calculated for each event by summing up the appropriately weighted energies found in each individual PPD and Ring Calorimeter channel. The weights are given by $\sin\vartheta$, with ϑ being determined in the PPD from the wire distance from the beam, and in the Ring Calorimeter by the distance from the center of a cell to the beam, relative to the distance from the target to the respective calorimeter, taking into account the average shower development in depth. The cartesian PPD readout geometry [7], [10] was corrected for by an overall factor of $\pi/4$.

Preliminary E_T spectra presented at Quark–Matter 1987 [11] were not corrected for leaking electromagnetic shower energy from the PPD. For electrons, the fraction extending into the Ring Calorimeter is small. For photon showers, which on average start to develop later, the leakage is considerably higher at the energies with which we are concerned. We simulated the fraction leaking from the PPD for nucleus–nucleus collisions using Fritiof–generated events. We found no dependence on the projectile–target system or on centrality of the collisions.

The electromagnetic shower energy seen by the Ring, and the fraction of hadronic shower energy seen in the PPD were corrected for the effect that the PPD (Ring) was calibrated for electromagnetic (hadronic) showers. This was done by taking into account the known e/π ratios, 1.49 for the PPD and 1.6 for the Ring Calorimeter. Electromagnetic E_T was extracted for the PPD acceptance (see Fig. 2) and hadronic E_T for the (slightly different) Ring acceptance. The corresponding fraction of hadronic E_T seen by the PPD is added to the Ring. Conversely, the electromagnetic E_T leaking from the PPD that actually went into the Ring was removed from the hadronic signal.

No attempt was made to reconstruct individual showers in the calorimeters. Instead, the effect of the shower spread in the response of the different rings was obtained from a Monte Carlo study together with a parametrization of the lateral shower spread. The shower profiles in the Ring Calorimeter for the hadron calibration at 10 GeV as a function of the radial distance from the calorimeter center were found to be best fitted with a sum of a delta–function at the shower center and an exponential. The lateral extension of hadronic shower does not change much with energy. Therefore a fixed profile parametrization was used for the simulation: $f(r) = c_1 \cdot (\delta(r - r_0) + c_2 \cdot e^{-|r-r_0|/c_3})$ with r_0 the radial calibration beam position, c_1 for overall normalization, $c_2 = 0.25$ and $c_3 = 8.2$ cm. The combination of the shower spread with the radial energy gradient results in an effective energy transport from the inner to the outer rings. The energy gradient depends on the projectile–target system and on the centrality of the collisions. Therefore, correction factors

for the individual rings were extracted for central collisions separately for each projectile–target configuration to optimize the result in the region of the spectra of most interest. Large effects of up to 28% (in this case for the inner ring) were observed. These corrections were applied when calculating the total E_T and the E_T in each ring. The overall result is that E_T decreases. The final analysis of our data, presented here, thus leads to transverse energies lower by approximately 20%, compared to a preliminary report [11].

We found that the finite energy resolution of the calorimeters had no significant effect on the E_T spectra by comparing Fritiof events with and without response fluctuations. Consequently no special unfolding of the experimental spectra was necessary.

In order to calculate the pseudorapidity distributions $dE_T/d\eta$ the information from the Ring Calorimeter (with $\Delta\eta = 0.166$ in each ring) and from the PPD with its cartesian readout had to be combined. The PPD response was unfolded in an iterative way. Starting from the assumption of a flat pseudorapidity distribution the result of the first unfolding was used to extract a linear dependence on pseudorapidity as input for the second iteration. Information from each wire results in pseudorapidity density information at a pseudorapidity that corresponds to an energy–weighted mean radius attributed to the given wire. This simple and fast procedure was checked by a more time–consuming method that started from an appropriate parametrization of a pseudorapidity distribution and calculated wiremaps for the PPD that were then employed with the experimental data. A fit procedure varied the parametrization until the wiremaps agreed. Distributions found by this method agreed well with the results of the simpler procedure. Thus, all pseudorapidity distributions shown here were extracted by the fast algorithm. Pseudorapidity distributions for electromagnetic E_T extracted for the PPD have been corrected for leakage of electromagnetic showers and for contributions from hadronic showers that had started already in the PPD. The difference between hadronic E_T in the PPD and electromagnetic E_T leaking into the Ring Calorimeter was added to the Ring Calorimeter signals in determining the pseudorapidity distributions of hadronic E_T.

The systematic error in the total E_T scale is estimated to be 5%, while the scales in the electromagnetic and hadronic E_T spectra are uncertain by 10%.

4 Results

4.1 Spectral shapes of Forward and Transverse Energy.

The Veto Calorimeter energy spectra (E_{Veto}) are shown in Fig. 3. The opening in the Intermediate Calorimeter that served as an aperture for the Veto Calorimeter was 60 x 65 mm^2 at an effective distance from the target of 8.0 m (6.6 m) for 200 (60) GeV/nucleon. The E_{Veto} spectra for sulphur on different targets (S, Cu, Ag, Au) and oxygen on Au at 200 GeV/nucleon are shown in Figs. 3 a, b, and for oxygen on Cu, Ag and Au at 60 GeV/nucleon in Fig. 3 c. All E_{Veto} spectra shown

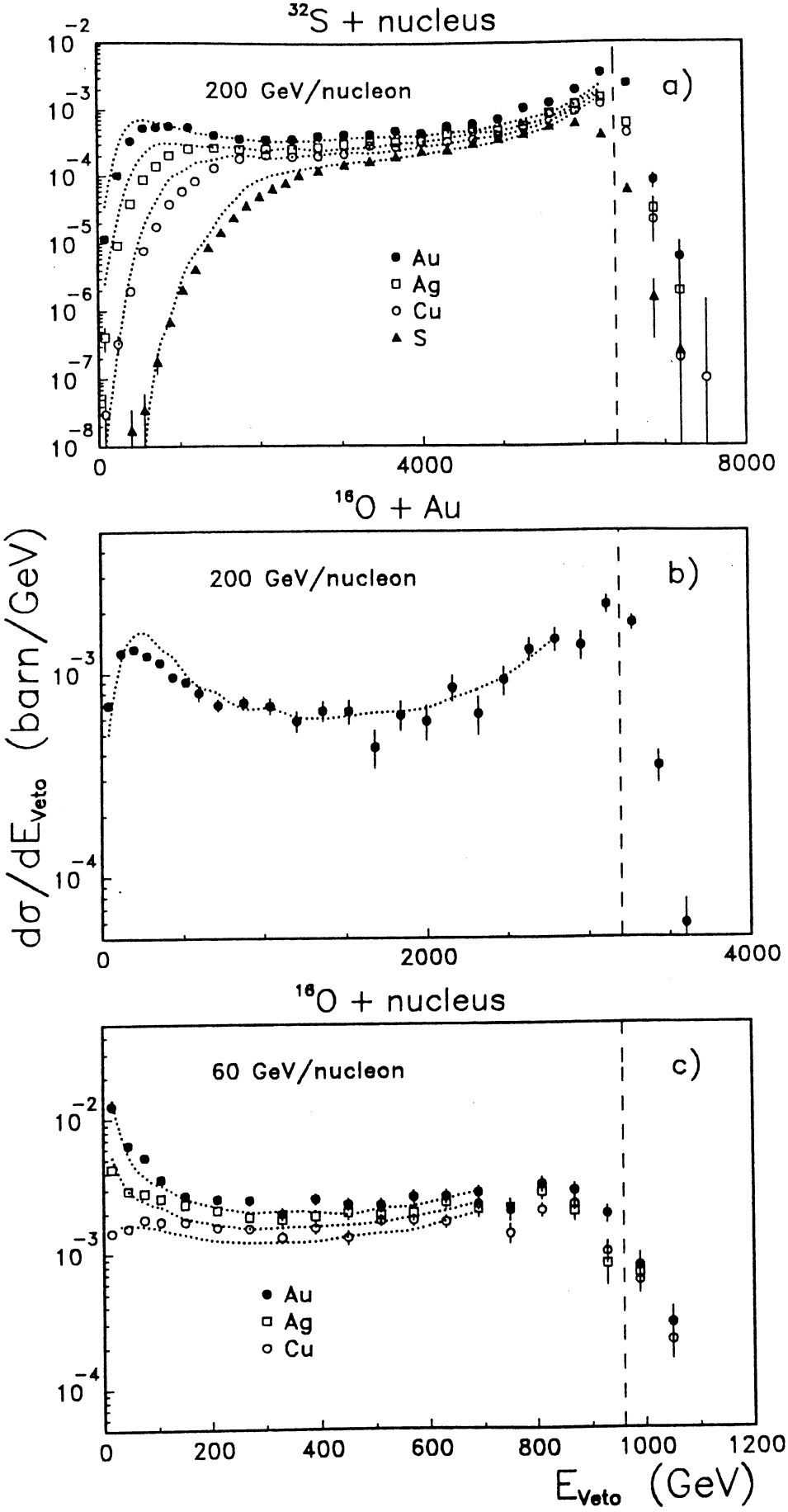

Figure 3 Energy spectra in the Veto Calorimeter for a) S+Au, Ag, Cu, S at 200 GeV/nucleon b) O+Au at 200 GeV/nucleon and c) O+Au, Ag, Cu at 60 GeV/nucleon. Fritiof spectra are shown with dotted lines for comparison. Close to the beam energy (dashed vertical line) the spectra strongly depend on the interaction trigger condition.

here were taken with the minimum bias interaction trigger.

The difference in collision geometry for various target sizes results in different probability distributions for the projectile nucleons to remain spectators during the interaction. This fact is reflected by the E_{Veto} spectra because projectile spectators are the main contribution to the E_{Veto} signal. For the O+Au system a central collision peak is seen at low E_{Veto} values. This peak is less pronounced in S+Au due to the lower probability for complete dive–in. In going to lighter target nuclei we end up with no chance to get zero Veto energy in the case of S+S. The probability for having almost no energy going forward is higher for 60 GeV/nucleon than for 200 GeV/nucleon.

A comparison with Fritiof (curves in Fig. 3) shows general agreement with the measured E_{Veto} spectra. The Fritiof simulation does not take into account leaking shower energy, from the material serving as aperture for the Veto calorimeter, that reaches the detector in addition to the particles going directly there. This results in higher probabilities for low Veto energies for the Fritiof simulation as seen in Figs. 3 a, b. E_{Veto} and E_T are anti–correlated and controlled by the impact geometry of a collision. This will be discussed in detail below. Central collisions lead to low E_{Veto} and high E_T. The technique of triggering on low E_{Veto} or high E_T has been used widely to select central collision events when studying other observables.

Differential transverse energy distributions for sulphur and oxygen projectiles at 200 GeV/nucleon and oxygen at 60 GeV/nucleon interacting with Au, Ag and Cu target nuclei are given in Fig. 4. The shapes are characterized by a rapidly decreasing cross section at low E_T (peripheral collisions), followed by a long plateau which ends in a steep fall–off.

The spectra extend to higher transverse energy values for larger target nuclei. They also change in shape as can be seen in Fig. 5, which illustrates the target dependence of the E_T distribution. In going from S+S (O+Al) to S+Au (O+Au), the shoulder becomes more pronounced. The E_T spectra for light–projectile/heavy–target collisions have been qualitatively understood in terms of impact geometry. They exhibit the contributions of grazing collisions at low E_T, followed by the domain of partial diving of the projectile into target matter, which produces the 'plateau'. It ends with the geometry of complete diving, $b = R_{target} - R_{proj.}$, at which point we expect the spectral slope to become steeper. Another characteristic point on the E_T scale might coincide with central collisions, $b \rightarrow 0$. The cross section should fall steeply from here on, a further increase in the total E_T occurring only as the result of fluctuations at the microscopic level. The simple idea thus arises to read off, from the spectra, the two characteristic quantities E_T^{DI} and E_T^{B0} where DI indicates complete diving and B0 near zero impact parameters. The latter value, in particular, would be of interest for an estimate of the effective stopping power and of the energy density. One would thus like to systematically determine E_T^{B0}, as a function of target and projectile mass, and of incident energy. We shall attempt below to understand the data in this qualitative manner but will first note several difficulties encountered with the concept of characteristic points along the E_T spectra:

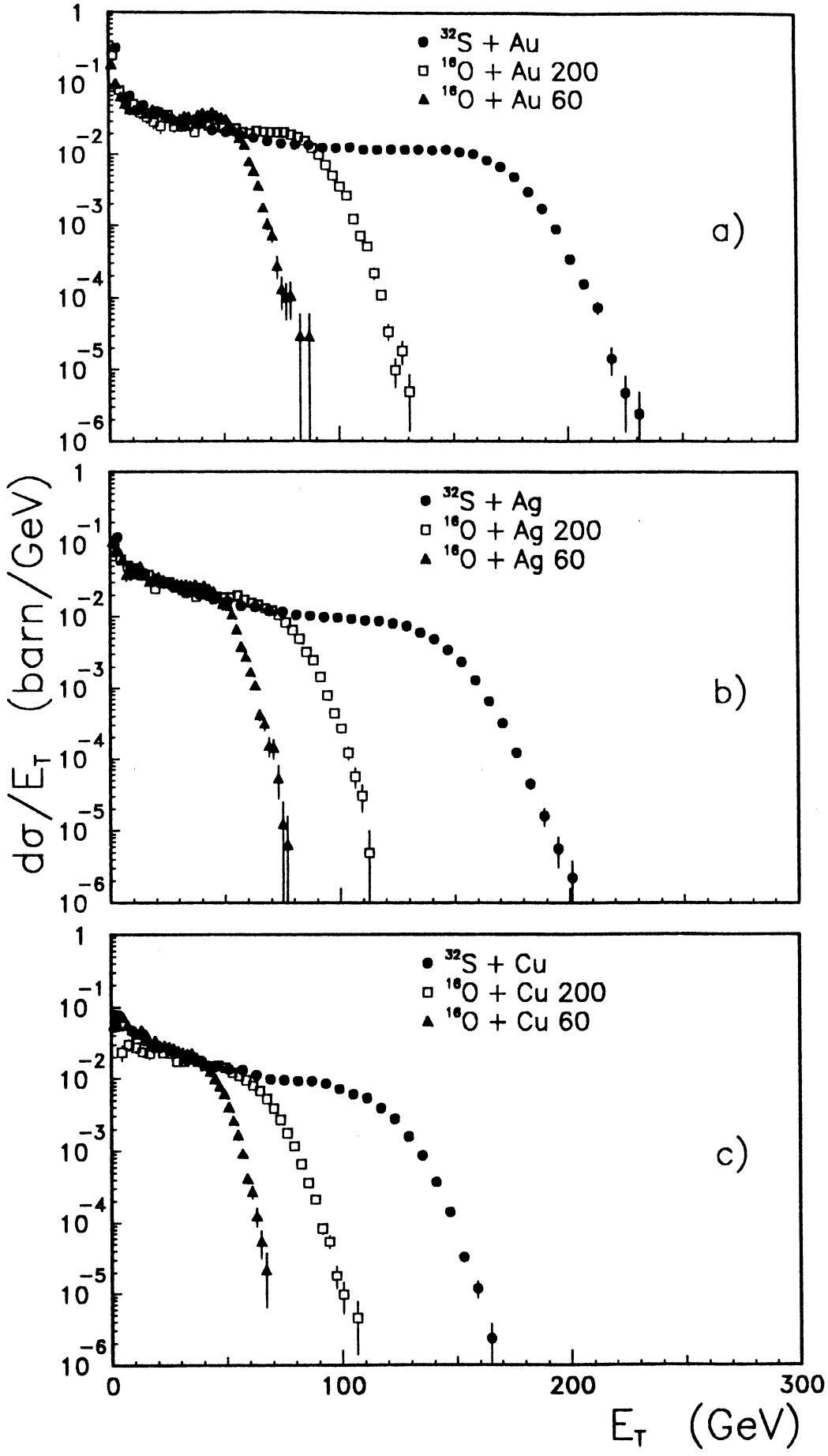

Figure 4 Transverse energy spectra, $d\sigma/dE_T$, for ^{32}S and ^{16}O projectiles, at 200 GeV/nucleon and for ^{16}O at 60 GeV/nucleon for a) Au, b) Ag, and c) Cu as target.

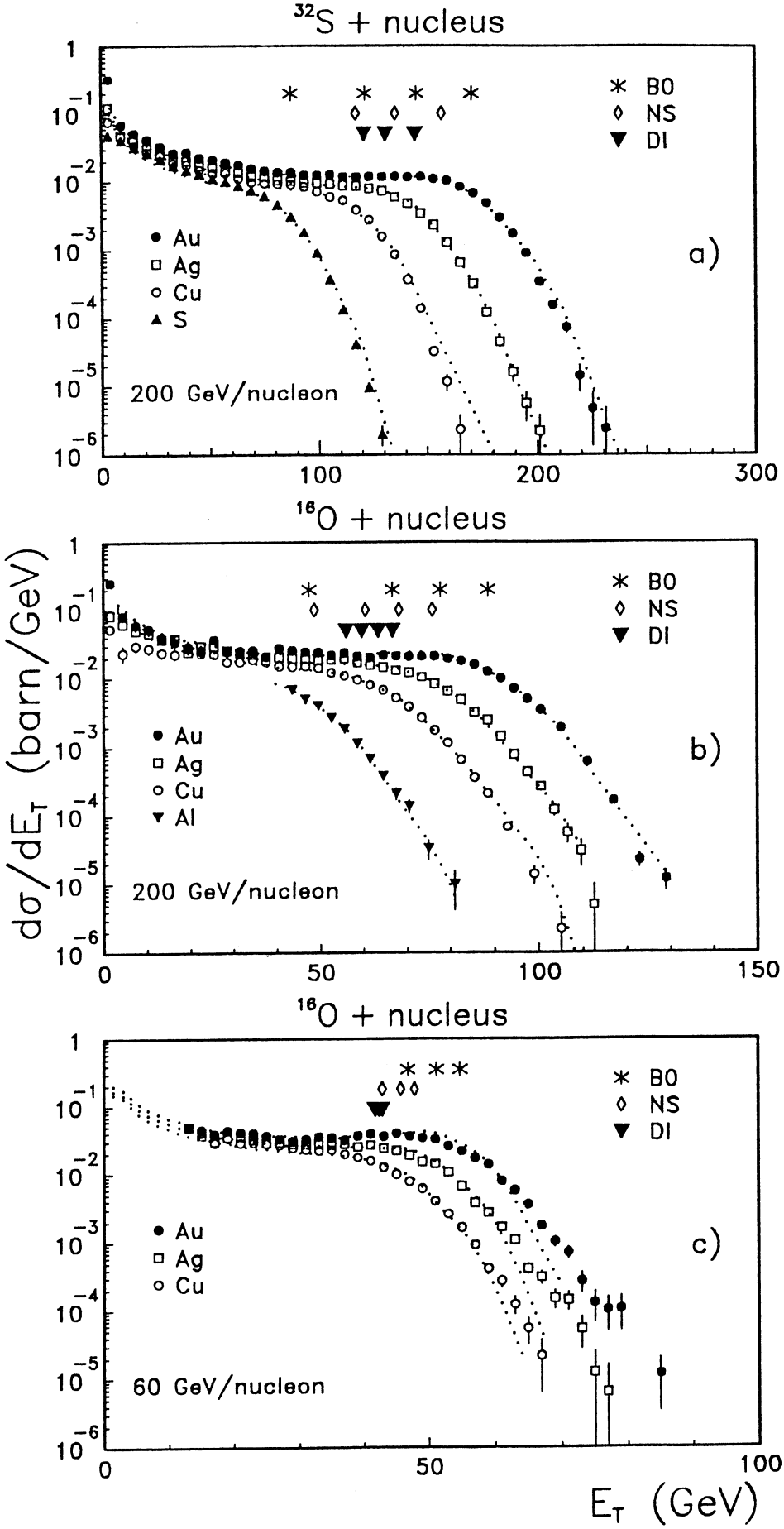

Figure 5 Transverse energy spectra, $d\sigma/dE_T$,with E_T as sum of E_T^{EM} and E_T^{HAD}, where E_T^{EM} is seen in PPD acceptance and E_T^{HAD} in Ring acceptance. a) for S+Au, Ag, Cu, S at 200 GeV/nucleon; b) for O+Au, Ag, Cu, Al at 200 GeV/nucleon; c) for O+Au , Ag, Cu at 60 GeV/nucleon. For comparison Fritiof results are shown as dotted lines with Fritiof scaled by factors given in Table 3 (see text). E_T values marked by (▼), (◇) and (∗) correspond to DI (complete dive-in), NS (no spectator going to Veto) and B0 (impact parameter b < 0.2 fermi) as explained in the text.

1. The variation of the spectral shapes with the masses both of projectile and target nuclei, render a systematic identification of characteristic points rather ambiguous.

2. At lower incident energies, such as at 60 GeV/nucleon employed in the present study, and at the yet lower energy of BNL experiments, all spectra are narrower and do not widen much in the high E_T domain after a certain target mass is reached.

3. Several problems, of a more technical nature, arise from a finite, non–4π calorimeter acceptance ($2.3 < \eta < 3.8$ in our case, see Fig. 2). The shapes of E_T spectra depend on the pseudorapidity window, an effect superimposed on the systematic variation of the spectral features in 4π with the collision geometry. Furthermore, a downward shift occurs in the effective rapidity of the center of mass of light–projectile/heavy–target collisions, in going from peripheral to central collisions. Recording E_T in a fixed, finite acceptance leads to complicated effects on the spectral shape, stemming from the shift of the center of mass relative to the acceptance.

The first two of the above aspects are obvious from Fig. 5 which shows the systematics of E_T spectra with target/projectile mass and incident energy. The ^{32}S+Au spectrum at 200 GeV/nucleon exhibits the broad structure described above, with an abrupt change from the plateau into the tail section. The central collision point, E_T^{B0}, may fall slightly above 160 GeV, with an uncertainty of approximately $\pm$ 15 GeV (10%). In the ^{16}O+Au reaction at 200 GeV/nucleon, however, the transition region from plateau to tail is much broader and all E_T^{B0} estimates are accordingly less accurate. Moreover, it is clear from the spectral shapes of reactions with lighter targets, in particular ^{32}S+S or ^{16}O+Al at 200 GeV/nucleon, that no characteristic points can be determined with reasonable accuracy. The O+nucleus data at 60 GeV/nucleon, finally, exhibit a smaller relative variation of the tail E_T with the target mass. In going from ^{64}Cu to ^{197}Au the tail shifts upwards by about 15 GeV only. No characteristic point could be determined to better than $\pm$ 6 GeV.

It is clear from the above considerations that the intuitive definition of characteristic E_T values is unsatisfactory. We thus choose to introduce more elaborate procedures to determine the transverse energy corresponding to full diving and central collisions, E_T^{DI} and E_T^{B0}. Fig. 5 shows overall agreement of the Lund–string model Fritiof with the data. We thus base the determination of characteristic E_T values in the experimental data on Fritiof calculations with various impact parameter choices. Fig. 6 illustrates Fritiof E_T spectra for S+Au at 200 GeV/nucleon, calculated for

(a) Minimum bias conditions;

(b) No projectile spectator nucleon remaining (closely related to full diving);

(c) Head on collisions ($b \cong 0$)

The Fritiof cross sections for these selections are listed in Table 2.

We adopt three different strategies for the purpose of obtaining estimates for characteristic E_T values that correspond to certain simply–defined impact geometries:

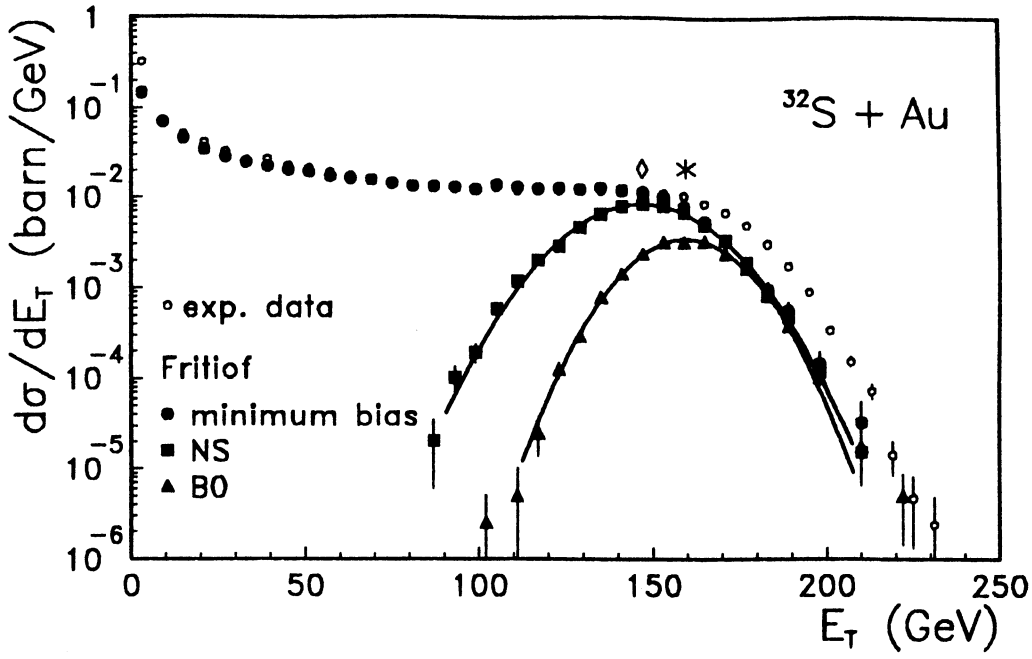

Figure 6 Fritiof generated transverse energy spectra for S+Au at 200 GeV/nucleon for B0 and NS conditions together with gaussian fits. Mean values are marked with (∗) for B0 and (◇) for NS. Normalization for B0 is arbitrary. The unbiased spectrum is shown as reference, together with the experimental distribution.

System	σ_{TOT} (param.)	σ_{TOT} (Fritiof)	σ_{DI}	σ_{NS} (Fritiof)
200 GeV				
S+Au	4.02	3.92	0.35	0.36
S+Ag	3.05	2.93	0.12	0.13
S+Cu	2.42	2.33	0.03	0.06
200 GeV				
O+Au	3.35	3.24	0.52	0.62
O+Ag	2.47	2.38	0.23	0.27
O+Cu	1.90	1.84	0.10	0.13
O+Al	1.27	1.22	0.01	0.04
60 GeV				
O+Au	3.35	3.25	0.52	0.60
O+Ag	2.47	2.37	0.23	0.27
O+Cu	1.90	1.84	0.10	0.13

Table 2 *Total*, *DI* and *NS* cross sections in barn for Fritiof and the mean value of the parametrizations which fit our data, described in [12].

I) For the interacting nuclei we assume homogeneous spheres with radii $\propto A^{1/3}$. The probability for a reaction to occur with complete dive–in is given by $P = \left(\frac{A^{1/3}-B^{1/3}}{A^{1/3}+B^{1/3}}\right)^2$ with A, B being the atomic mass numbers for target and projectile. The cross section for complete dive–in, DI, is defined by $\sigma_{DI} = P \cdot \sigma_{total}$. Typical values of σ_{DI} are 0.35 (S+Au), 0.52 (O+Au) and 0.03 barn (S+Cu). For σ_{total}(A,B) we use the mean values of the two parametrizations given in ref. [12]. We now correlate E_T^{DI} to σ_{DI} by demanding $\sigma_{DI} = \int_{E_T^{DI}}^{\infty}(d\sigma/dE_T)dE_T$. E_T^{DI} is extracted from integrated E_T spectra where $\sigma_{INT}(E_T) = \int_{E_T}^{\infty}(d\sigma/dE_T')dE_T'$ is plotted as function of E_T. Following this procedure we extract E_T^{DI} for all projectile–target combinations for data and for Fritiof simulated E_T spectra.

II) For Fritiof generated E_T spectra (Fig. 6) that were selected with the constraint that no projectile spectator reached the Veto Calorimeter we extract the mean E_T value (E_T^{NS}(Fritiof), No Spectator). We can now determine the cross section σ_{NS} that corresponds to E_T^{NS}(Fritiof) in the minimum bias E_T spectrum. It is given by $\sigma_{NS} = \int_{E_T^{NS}(Fritiof)}^{\infty}(d\sigma/dE_T)dE_T$. As experimental and simulated spectra are very similar in shape and differ only slightly in scale it makes sense to extract E_T^{NS}(Data) by demanding $\sigma_{NS} = \int_{E_T^{NS}(Data)}^{\infty}(d\sigma/dE_T)dE_T$ for the experimental E_T spectrum.

III) Our third approach employs Fritiof spectra for $b < 0.2$ fermi, i.e. effectively zero impact parameter (B0). We extract E_T^{B0}(Fritiof) as the mean E_T values obtained in head–on collisions (Fig. 6). We determine σ_{B0} from the unbiased Fritiof spectra at E_T^{B0}(Fritiof) and, quite analogous to the NS case we obtain E_T^{B0}(Data) by $\sigma_{B0} = \int_{E_T^{B0}(Data)}^{\infty}(d\sigma/dE_T)dE_T$ for the experimental data.

All results from the three procedures above are listed in Table 3. The characteristic E_T values are also marked in Fig. 5.

In Tables 4 and 5 we show the ratios of these various E_T values. Table 4 compares the E_T values found at 60 GeV/nucleon to those at 200 GeV/nucleon, for the oxygen projectile. The calorimeters were moved closer to the target by 1.4 m for the 60 GeV runs. By this, the relative acceptance for the two energies was made sufficiently similar to yield identical shapes for the E_T spectra at 60 and 200 GeV/nucleon for each target (Cu, Ag, Au). The scaling factors for E_T that bring the 200 GeV/nucleon spectra to overlap with the 60 GeV/nucleon spectra are listed in Table 4. They are different for different targets and for E_T, E_T^{EM} and E_T^{HAD} (see next section). For the O+Au collision the factor is about 0.63 whereas the ratio of the available c.m. energies ($\sqrt{s}$ minus the net–baryon rest mass) is 0.50. As we shall see in more detail in chapter 5 the reason may be identified as a higher 'relative stopping power' at the lower energy: a larger fraction of $\sqrt{s} - n \cdot m_0$ (where n is the number of participating nucleons) is transformed into E_T.

Comparison of the E_T generated in S+nucleus collisions to that observed for oxygen projectiles is given in Table 5. The 'zero impact parameter' (B0) ratio of E_T(S+Au)/E_T(O+Au) at 200 GeV/nucleon is about 1.9, slightly higher than the Fritiof value of 1.80. This ratio is less than two, the value that one might intuitively assume. It is given rather by the total available energy

200 GeV	E_T			E_T^{EM}			E_T^{HAD}		
System	Data	Fritiof	D/F	Data	Fritiof	D/F	Data	Fritiof	D/F
	145	136	1.07	41.1	42.6	0.98	103	93.6	1.11
S+Au	157	147	1.07	44.7	45.5	0.98	112	101	1.10
	170	160	1.07	48.3	49.4	0.98	121	110	1.10
	131	127	1.03	37.2	39.8	0.94	93.6	88.0	1.06
S+Ag	135	131	1.03	38.3	40.9	0.94	96.3	90.6	1.06
	145	140	1.04	40.8	43.5	0.93	103	96.6	1.07
	121	117	1.04	34.8	37.5	0.93	87.0	81.2	1.07
S+Cu	117	113	1.03	33.0	35.3	0.94	84.0	77.8	1.08
	121	117	1.04	34.0	36.4	0.93	86.4	80.6	1.07
	–	–	–	–	–	–	–	–	–
S+S	–	–	–	–	–	–	–	–	–
	87.0	82.5	1.06	23.9	25.9	0.92	62.1	56.6	1.10

200 GeV	E_T			E_T^{EM}			E_T^{HAD}		
System	Data	Fritiof	D/F	Data	Fritiof	D/F	Data	Fritiof	D/F
	66.7	68.4	0.98	19.6	21.2	0.93	46.4	47.0	0.99
O+Au	75.9	76.6	0.99	22.5	23.9	0.94	53.1	52.7	1.01
	88.6	88.5	1.00	26.1	27.5	0.95	61.5	60.9	1.01
	63.3	64.7	0.98	18.6	20.3	0.92	44.4	44.6	1.00
O+Ag	68.2	69.8	0.98	20.2	21.8	0.93	48.0	48.0	1.00
	77.8	79.3	0.98	22.9	24.7	0.93	54.3	54.6	0.99
	59.5	61.2	0.97	17.5	19.5	0.90	42.3	42.2	1.00
O+Cu	60.4	62.2	0.97	17.5	19.5	0.90	42.7	42.7	1.00
	66.7	68.5	0.97	19.4	21.4	0.91	47.1	47.1	1.00
	55.9	55.6	1.02	16.6	18.6	0.89	40.4	39.2	1.03
O+Al	48.6	48.4	1.00	13.7	15.3	0.90	34.5	33.1	1.04
	47.4	47.3	1.00	13.3	14.9	0.90	33.6	32.4	1.04
60 GeV	E_T			E_T^{EM}			E_T^{HAD}		
System	Data	Fritiof	D/F	Data	Fritiof	D/F	Data	Fritiof	D/F
	42.8	44.3	0.97	13.7	13.3	1.03	29.0	30.9	0.94
O+Au	47.8	49.0	0.98	15.4	14.8	1.04	32.5	34.2	0.95
	54.8	54.5	1.00	17.1	16.4	1.05	37.0	38.2	0.97
	42.4	42.5	1.00	13.0	13.0	1.03	29.3	29.4	1.00
O+Ag	45.7	45.5	1.00	14.0	13.8	1.01	31.6	31.7	1.00
	51.2	50.2	1.02	15.4	15.1	1.02	35.1	35.1	1.00
	41.7	40.5	1.03	12.0	12.7	0.95	29.3	28.3	1.04
O+Cu	42.8	41.4	1.03	12.9	12.6	1.02	29.8	28.8	1.03
	46.8	44.9	1.04	13.9	13.6	1.02	32.4	31.3	1.04

Table 3 Transverse energy values in GeV (total, electromagnetic and hadronic) for DI, NS and B0 (first, second and third row of each system). For definitions see text. The experimental results are compared to Fritiof simulation.

Target		Au		Ag		Cu	
		Data	Fritiof	Data	Fritiof	Data	Fritiof
E_T^{TOT}	DI	.64	.65	.67	.65	.70	.66
	NS	.63	.64	.67	.65	.71	.67
	B0	.62	.62	.66	.63	.70	.66
E_T^{EM}	DI	.70	.63	.70	.64	.69	.68
	NS	.69	.62	.70	.63	.74	.65
	B0	.66	.59	.67	.61	.72	.64
E_T^{HAD}	DI	.62	.66	.66	.66	.69	.68
	NS	.61	.65	.66	.66	.70	.67
	B0	.60	.63	.65	.64	.69	.66

Table 4 Transverse energy scaling factors between 60 and 200 GeV/nucleon for oxygen projectiles. DI, NS and B0 ratios are compared to Fritiof.

Target		Au		Ag		Cu	
		Data	Fritiof	Data	Fritiof	Data	Fritiof
E_T^{TOT}	DI	2.17	1.98	2.07	1.96	2.03	1.90
	NS	2.07	1.92	1.98	1.88	1.94	1.82
	B0	1.92	1.80	1.87	1.77	1.82	1.71
E_T^{EM}	DI	2.09	1.99	2.00	1.96	1.99	1.93
	NS	1.99	1.91	1.90	1.86	1.89	1.82
	B0	1.85	1.79	1.78	1.76	1.75	1.70
E_T^{HAD}	DI	2.23	1.99	2.11	1.97	2.06	1.92
	NS	2.11	1.93	2.01	1.89	1.97	1.82
	B0	1.97	1.81	1.90	1.77	1.83	1.71

Table 5 Transverse energy scaling factors between sulphur and oxygen projectiles. DI, NS and B0 ratios are compared to Fritiof.

$(\sqrt{s} - n \cdot m_0)$, which increases by 1.77 for ideal head–on O+Au and S+Au collisions.

Concerning the other entries in Table 5 the ratio is expected to approach 2.0 if we consider a complete dive–in geometry rather than just head–on collisions (because the target/projectile participant nucleon numbers approach each other), and if we choose heavier targets. This trend is seen clearly in Table 5, both in the data and in Fritiof. A slight systematic overestimation of the E_T scale in the data, observed with sulphur projectiles, may be responsible for the scaling values above 2.0, particularly in the case of the Au target.

We end this section with a detailed comparison of E_T spectra obtained at different energies, and with different projectiles. Fig. 7 (left column) gives the spectra for oxygen–induced reactions at 60 and 200 GeV/nucleon, respectively. The E_T scale is normalized to the dive–in (DI) values of E_T obtained for each reaction (c.f. Table 3). With this scaling, very little dependence on the incident energy is seen in the shapes. The spectra for the Au target extend much farther, beyond $E_T = E_T^{DI}$, than for lighter targets. This effect follows from simple impact parameter geometry: dive–in occurs at $b = 4.1$ fm for O+Au but at $b = 1.8$ fm in O+Cu using a sharp sphere model. Thus a higher fraction of the total cross section is observed with $E_T > E_T^{DI}$ in O+Au than in O+Cu collisions.

Fig. 7 also gives a comparison of E_T spectra for sulphur and oxygen projectiles (right column). The same normalization to E_T^{DI} is employed here. Drastic shape differences are obvious, both at low and, particularly, at high E_T values. The distributions for the sulphur projectile fall off much faster after reaching the shoulder at $E_T/E_T^{DI} \approx 1.1$. The steeper slopes at higher E_T for sulphur have an intuitive statistical explanation: after reaching near–zero impact parameter, the 32 nucleons produce an average $< E_T^{32} > \approx 2 \cdot < E_T^{16} >$, the corresponding quantity for the oxygen projectile. In order to increase E_T further we must consider fluctuations of the E_T created by each incoming nucleon. In order to fluctuate up to, say, $1.2 \cdot < E_T >$, the 32 sulphur nucleons together would have to deposit *twice* the extra energy than the 16 oxygen nucleons. However, the mean width of fluctuation increases by $\sqrt{2}$ only as the ensemble gets doubled. Thus, although the tail slope decreases with projectile mass, on an absolute E_T scale (c.f. Fig. 4), it gets steeper on the relative E_T/E_T^{DI} scale of Fig. 7. The same behaviour would arise in a 16– and 32– fold convolution, respectively, of the E_T spectrum observed in inelastic p+Au collisions: the mean would go up twice in the latter case, but the relative rms would be reduced by $\sqrt{2}$. We shall return to the question of a description in terms of independent projectile nucleon interactions in the target in sect. 6.

4.2 Electromagnetic and Hadronic E_T–distributions

Turning to an analysis of the fractions of total E_T contained in electromagnetic and hadronic showers, we note first that in the decay of an isospin symmetric pion gas the ratio E_T^{EM}/E_T^{HAD} is 0.5, whereas it is lowered in all realistic multiparticle final states, due mainly to the presence of

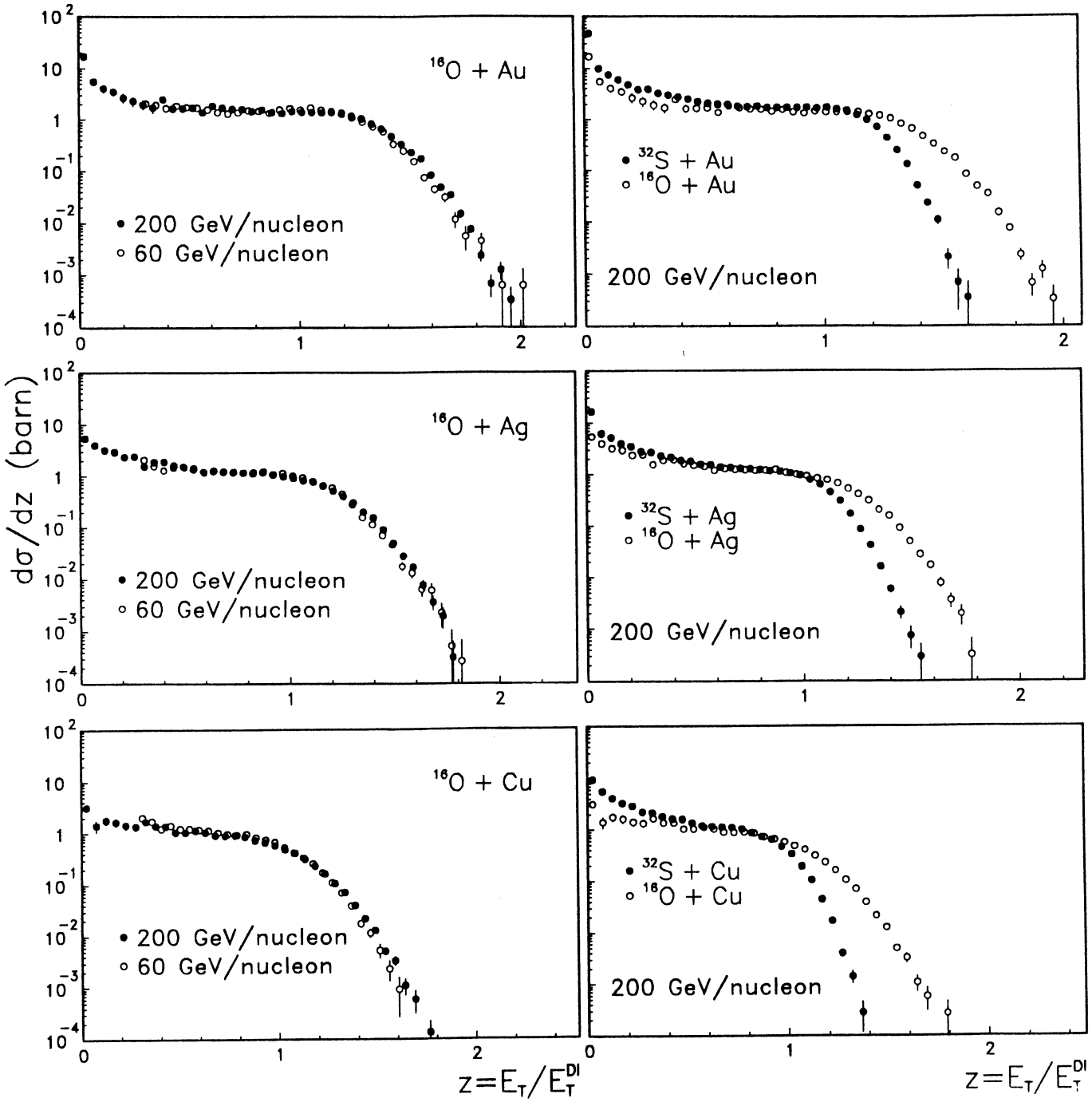

Figure 7 Transverse energy spectra for O+Au, Ag, Cu at 60 and 200 GeV/nucleon (left column) scaled by E_T^{DI} (see Table 3) to show the similarity in shape for the two energies. Transverse energy spectra for S and O on Au, Ag, Cu at 200 GeV/nucleon (right column) scaled with corresponding E_T values at DI given in Table 3. Tables 4 and 5 give a complete list of the corresponding scaling factors.

baryons. In ultra–relativistic nucleus–nucleus collisions this ratio is of interest both at the event–by–event and at the ensemble average level. Exotic events of the 'Centauro' type [13] would constitute a very rare fraction of central collision events but with a drastic departure away from the 'standard' ratio of approximately 0.45 observed in hadron–hadron collisions. Even a relatively modest reduction in the average central collision ratio would also be of interest. It might indicate a shift in the final state of hadron composition, from pion production toward the production of strange mesons, hyperons, and baryon–antibaryon pairs. In fact, an enhancement of $K, \Lambda, \overline{\Lambda}$ and ϕ in central nucleus–nucleus collisions has been observed recently [14], [15].

The differential distributions for the electromagnetic (left) and hadronic (right) parts of E_T are displayed in Fig. 8. The overall systematics of the shapes, discussed in the previous section, are also exhibited by the EM spectra. However, the spectra for electromagnetic transverse energy (E_T^{EM}) and total transverse energy (E_T) do not agree well in shape as seen in Fig. 9, where the data are plotted for various projectile–target systems scaled by the dive–in transverse energy $E_T^{DI(EM)}$. For electromagnetic spectra the peak or shoulder around $z = 1$ (i.e. E_T^{EM}=$E_T^{DI(EM)}$) tends to be less pronounced, balanced by a tail that extends to higher relative E_T values. The effect is less clearly visible for lighter targets since we scaled with the DI value of E_T^{EM}, which shifts farther towards the tails of the spectra for lower target mass. The difference between electromagnetic and hadronic spectra is reproduced well by Fritiof (curves in Fig. 8). The different shape for E_T^{EM} is not a result of the slight difference in acceptance between the PPD and the Ring Calorimeter. It is, in part, a consequence of baryonic contributions to E_T. Furthermore, E_T^{EM} is a small fraction of total E_T and thus fluctuates more. This was verified by Fritiof studies changing acceptance, removing the baryonic content from E_T and comparing $E_T(\pi^+, \pi^-)$ with $E_T(\pi^0)$.

We turn now to the ratio E_T^{EM}/E_T^{HAD} recorded event by event in the common acceptance of PPD and Ring. The experimental distribution for S+S collisions is shown in Fig. 10. We see that the correlation between E_T^{EM} and E_T^{HAD} is quite strong in the data. This had to be expected given the fact that the showers extend over both calorimeter parts. E_T^{EM} and E_T^{HAD} from the experiment are corrected for this shower spread *only* on average but not on an event by event basis. At the level of available statistics, Fig. 10 shows no exotic, low cross section events with excursion far away from the mean ratio.

Mean values are given for E_T^{EM}/E_T^{HAD} in Table 6 both for experimental data and Fritiof simulations. The event ensembles from which this ratio was obtained, as an average over event–by–event ratios, were selected to include only the central collision fraction by requiring $E_T > E_T^{DI}$. The corresponding DI values of E_T are those listed in Table 3, both for the data and Fritiof ensemble selections. We adopted this selection procedure, instead of the model independent comparison of E_T^{EM} and E_T^{HAD} from the corresponding minimum bias event samples, in order to enhance the signal of possible effects associated with central collisions. The average experimental mean values

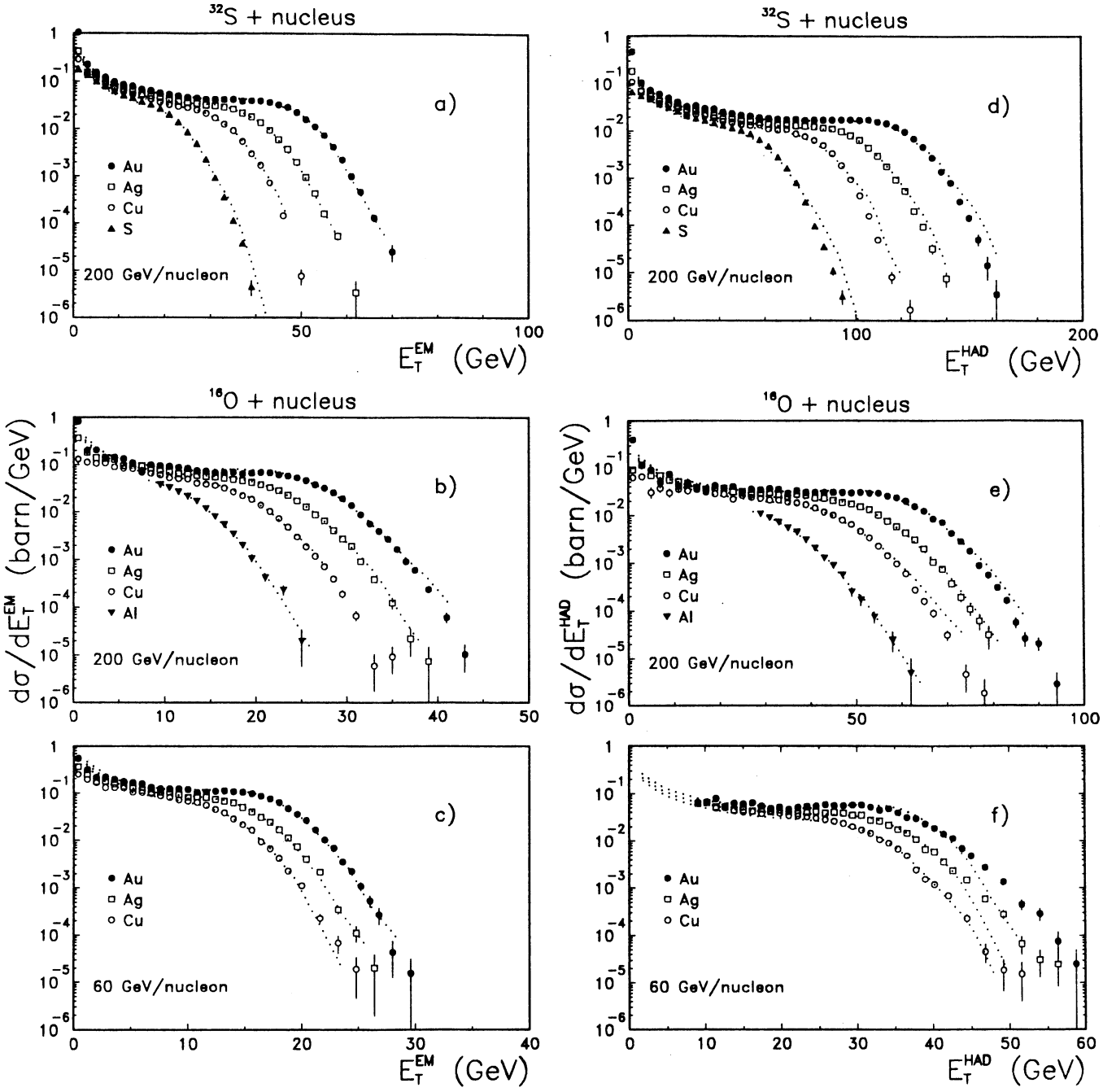

Figure 8 Differential cross section distributions for E_T^{EM} (left) and E_T^{HAD}(*right*) (E_T^{EM} in PPD and E_T^{HAD} in Ring acceptance). a), d) for sulphur and b), e) for oxygen at 200 GeV/nucleon; c), f) for oxygen at 60 GeV/nucleon. For comparison Fritiof results are shown as dotted lines with Fritiof scaled by factors given in Table 3 (see text). Corresponding values for DI (complete dive–in), NS (no spectator going to Veto) and B0 (impact parameter b < 0.2 fermi) are given in Table 3.

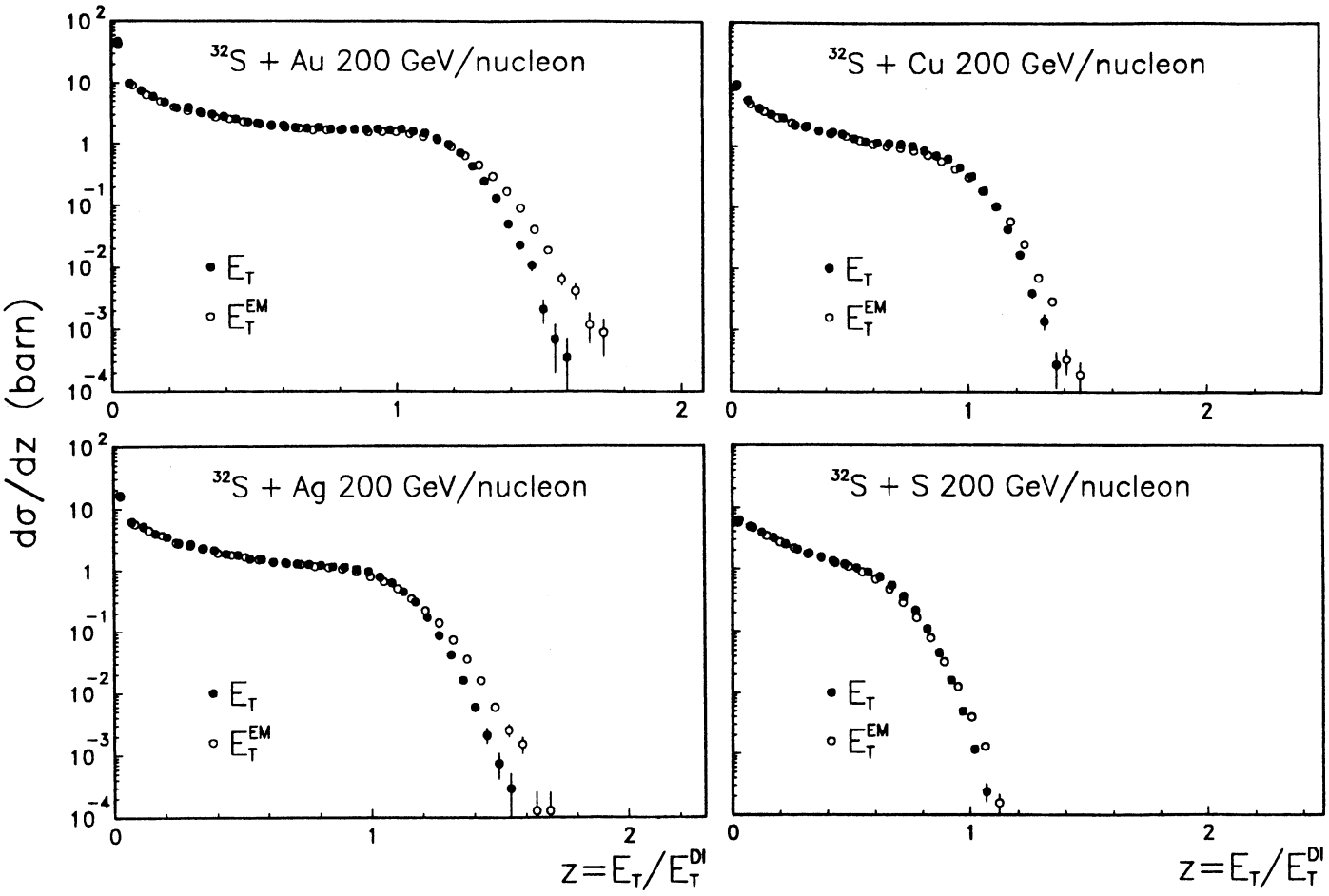

Figure 9 Comparison of transverse energy spectra for $E_T \leftrightarrow E_T^{EM}$ for S+Au, Ag, Cu, S. Spectra have been scaled with corresponding E_T values for complete dive-in (DI).

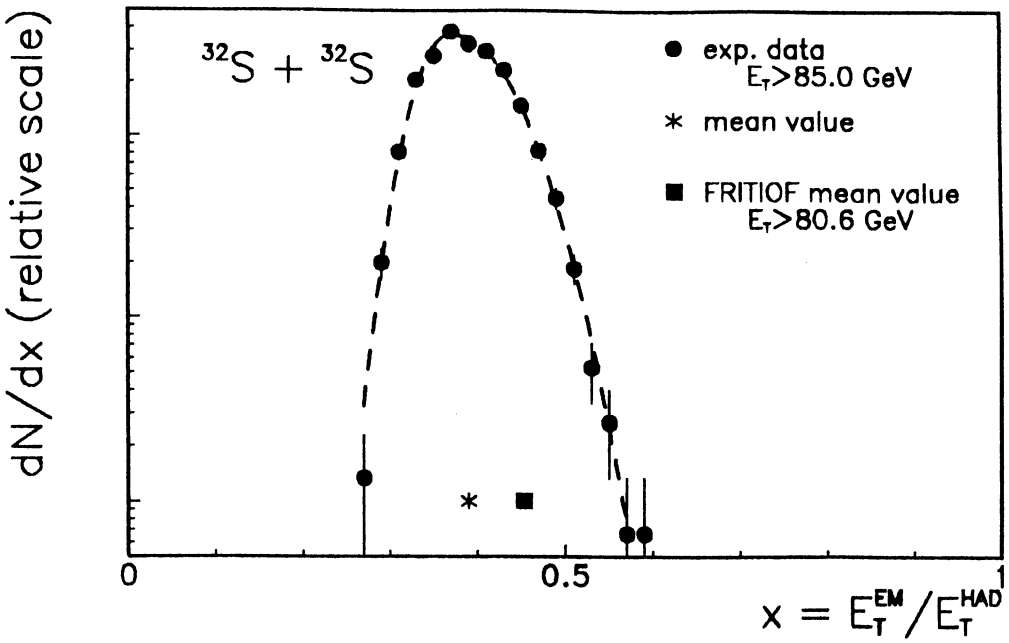

Figure 10 Experimental E_T^{EM}/E_T^{HAD} distributions with fit (dashed curve) for S+S 200 GeV/nucleon with $E_T > 85$ GeV. For data (Fritiof) we extract a mean value of 0.39 (0.45) GeV and rms value of 0.049 (0.085) GeV. For other target–projectile combinations see Table 6.

	Data			Fritiof			D/F	D/F
System	mean	rms	ratio	mean	rms	ratio	mean	rms
S+Au	.40	.037	.093	.45	.061	.137	.90	.68
S+Ag	.39	.040	.101	.45	.063	.140	.88	.72
S+Cu	.40	.041	.103	.45	.069	.155	.89	.67
S+S	.39	.046	.119	.45	.085	.187	.86	.64
200GeV								
O+Au	.43	.056	.130	.46	.083	.181	.95	.72
O+Ag	.42	.064	.152	.45	.089	.197	.93	.77
O+Cu	.41	.066	.159	.45	.093	.205	.91	.77
O+Al	.39	.070	.178	.47	.087	.187	.85	.81
60GeV								
O+Au	.47	.082	.173	.43	.092	.212	1.09	.89
O+Ag	.45	.088	.193	.43	.094	.216	1.05	.94
O+Cu	.46	.078	.167	.44	.101	.230	1.06	.77

Table 6 Mean and rms values for E_T^{EM}/E_T^{HAD} distributions with cuts in E_T at E_T^{DI} for the Data and Fritiof.

of E_T^{EM}/E_T^{HAD} are about 0.40 $\pm$ 0.04 for sulphur–induced central collisions, and 0.42 $\pm$ 0.06 for oxygen–induced collisions at 200 GeV/nucleon. These values are systematically lower by about 10% than the corresponding Fritiof results.

4.3 Pseudorapidity Distributions of Transverse Energy

We now turn to the dependence of E_T on η, in the expectation of finding the specific kinematics of light–projectile/heavy–target collisions reflected in systematic shifts of the pseudorapidity distributions, $dE_T/d\eta$, both with the target mass and with the centrality of the collisions. Our comparisons of η–integrated data to the Fritiof model in section 4.1 showed overall agreement of theory and data: the total energy deposition and stopping power (see below) seems to be well described by the Fritiof assumption of successive leading baryon re–interactions along its trajectory. Comparison to differential data in pseudorapidity will test the model at a more sensitive level.

We also investigate the η–dependence of E_T in order to pin down possible artifacts or distortions in the stopping power systematics, resulting from a finite, non–4π acceptance. This is not so important for equal–mass systems like S+S as in O+Au or S+Au where the maximum $dE_T/d\eta$ shifts relative to the fixed acceptance. We will, therefore, prepare in this section the methods for overcoming the effects of limited acceptance by the following three approaches:

1. Extrapolate $< E_T >$ values to 4π acceptance, employing $dE_T/d\eta$ distributions obtained from the Fritiof model.

2. Concentrate on the transverse energy density $dE_T/d\eta(\eta = y_{cm})$ in the vicinity of the c.m. rapidity, coinciding closely with the maximum of the pseudorapidity distribution, i.e. consider the A systematics of $(dE_T/d\eta)_{max}$. As our acceptance contains this maximum, finite–acceptance effects are thus eliminated.

3. From a comparison of $(dE_T/d\eta)_{max}$ systematics with finite–acceptance, integrated E_T values (for dive–in, or central collision points), ascertain that the systematics of the latter leads to similar conclusions as the former.

In the stopping power analysis below (chapter 5) we shall see that consistent conclusions can thus be reached.

Pseudorapidity distributions depend on centrality and thus, on the total observed E_T, as demonstrated in Fig. 11 where bands in E_T were selected for O+Au and S+Au going from peripheral to central collisions. For E_T^{EM} we see the peak shifting, from a position near the nucleon–nucleon midrapidity (y=3.03) towards the values $\eta = y_{cm}$=2.44(2.57) expected for central (b=0) collisions of ^{16}O (^{32}S) on Au. The distribution becomes asymmetric as a consequence of an increasing ratio of target participant nucleons to projectile participants. For the S+Au data the experimental acceptance covers the peak regions of $dE_T/d\eta$ distributions quite well. This coverage is not quite so favourable in O+Au at 200 GeV/nucleon. In the 60 GeV/nucleon data (see Fig. 12) the peak

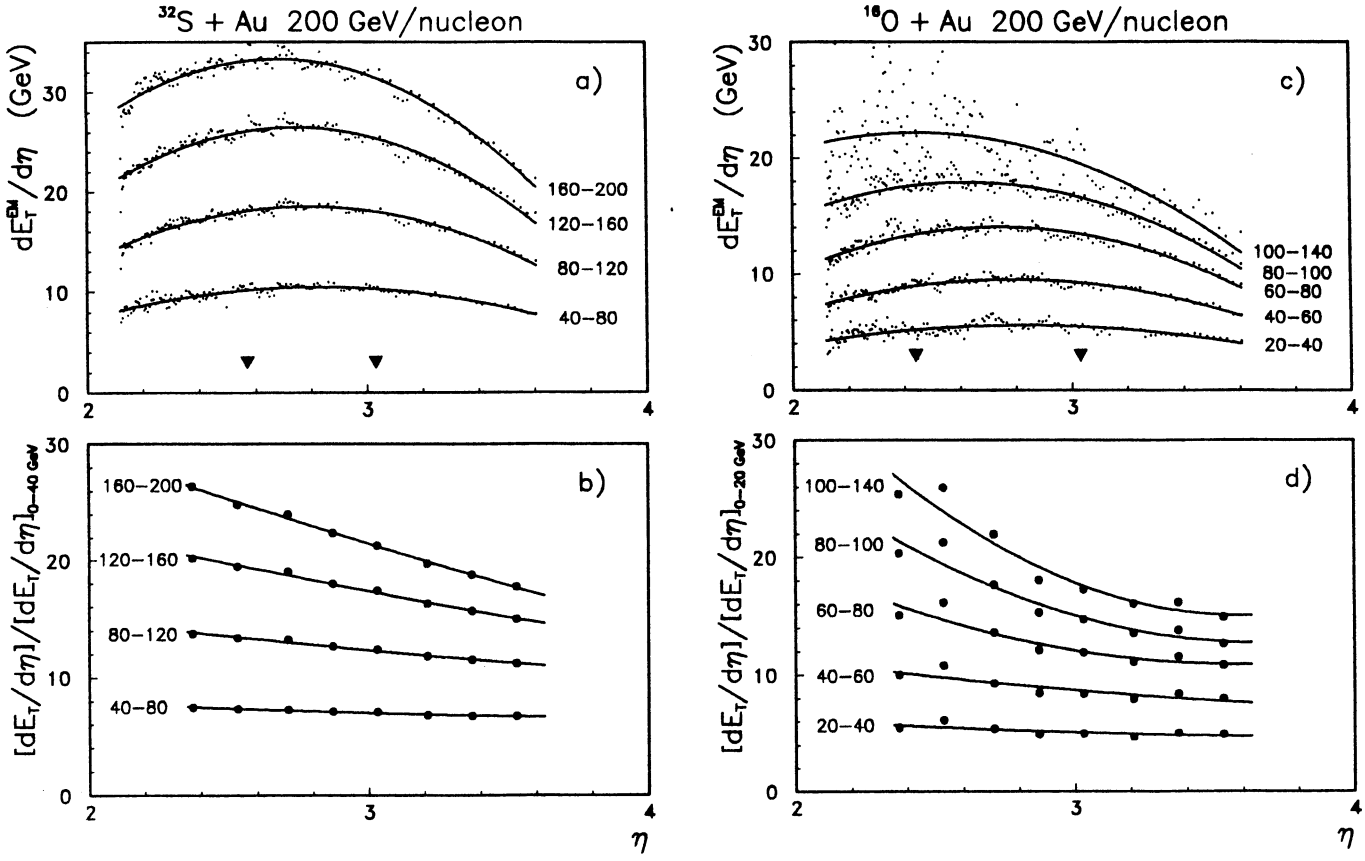

Figure 11 Pseudorapidity distributions for different bands in E_T for S+Au and O+Au at 200 GeV/nucleon. a), c) show $dE_T^{EM}/d\eta$ as extracted from PPD individual wire information (dots) together with fits (full lines). b), d) give $dE_T/d\eta$ distributions relative to the distribution for the lowest E_T band with fits. Indicated by full dots are pseudorapidities of the calorimeter rings. In a) and c) $\eta = y_{cms}$ values are marked (by triangles) for $b = 0$ and a symmetric target–projectile situation (see Table 9).

System	b (fermi) grazing collisions	b (fermi) Dive-In	$< b >_{DI}$ (fermi) $(= 2/3 \cdot b_{DI})$
S+Au	11.3	3.3	2.2
S+Ag	9.9	2.0	1.3
S+Cu	8.8	1.0	0.7
S+S	7.6	0.0	0.0
O+Au	10.3	4.1	2.7
O+Ag	8.9	2.7	1.8
O+Cu	7.8	1.8	1.2

Table 7 Impact parameter for complete Dive-In (DI) and grazing collisions assuming homogeneous spheres. The mean impact parameter for DI is used in Figs. 17 and 18 for comparison.

falls at the border of the acceptance for central O+Au collisions.

Taking the peripheral distributions as a reference to plot $dE_T/d\eta$ for the different bands in E_T relative to the lowest E_T band (Figs. 11 b, d) we see that, with increasing centrality, pseudorapidity densities rise faster for lower η as a consequence of the increasing asymmetry in number of projectile and target participants. This effect is reproduced by Fritiof as we shall demonstrate below. Fig. 12 shows the dependence of pseudorapidity distributions on the size of the target nucleus for central collisions which were selected to have $E_T > E_T^{DI}$. S+S events were selected by $E_T >$ 85 GeV because no complete dive–in occurs for symmetric collisions. Figs. 12 c, e give equivalent information on oxygen–induced collisions at 200 GeV/nucleon and 60 GeV/nucleon.

We also show ratio plots, similar to those in Fig. 11, for S+nucleus data relative to S+S and for the oxygen–induced reactions by normalizing to O+Al (200 GeV/nucleon) and O+Cu (60 GeV/nucleon) in Figs. 12 b, d, f. The S+S data and O + Al data are approximately symmetric about $\eta = 3.0$. For higher target masses the peak shifts to lower pseudorapidities[1].

This effect is geometric in origin and can be qualititatively reproduced by Fritiof, as seen in Fig. 13 which gives a comparison of E_T^{EM} pseudorapidity distributions for data and Fritiof predictions. We illustrate this for the reactions S+Au, Cu, and S at 200 GeV/nucleon, selecting $E_T > E_T^{DI}(E_T^{NS})$ for the data (Fritiof). We observe that the model predictions tend to peak at slightly higher η than the corresponding data. This effect may be the consequence of having omitted rescattering of the *produced* particles in Fritiof, visible in the data for the heavier target nuclei. With the exception of this shift of the maxima, by about $\Delta\eta = 0.5$, the agreement is reasonable, in view also of our systematic uncertainty in the unfolding of electromagnetic and hadronic E_T.

The data of Figs. 11 and 12 show a shift of the E_T pseudorapidity distributions both with increasing centrality of collision, and with increasing target mass (in central collisions). The variation of E_T with A thus depends on the rapidity domain considered. The O+nucleus data at 60 GeV/nucleon, in particular, show *no* dependence on A in the vicinity of $\eta = 3.5$. In general, the variation of E_T with A is the fastest at small pseudorapidity and disappears at a certain value $\eta_0 > y_{cm}$. This is obvious also from data presented by NA34 [16] for η distributions in the full phase space. In the discussion of the stopping power systematics one usually supposes an A^α dependence of E_T, with α obtained from fitting the target mass dependence. Obviously, α is a steep function of rapidity in light–projectile/heavy–target collision systems. This has to be kept

[1]Also indicated (by triangles) in Fig. 12 are the values of $\eta = y_{cm}(b = 0)$ for different projectile–target systems. We see that the observed peak positions follow the shift in the center of mass pseudorapidity. However, the selection $E_T > E_T^{DI}$ does not result in head–on collisions. Results of model calculations shown in Table 7 reveal that the average impact parameter $< b >_{DI}$ for the selection $b < b_{DI}$ increases with the target mass, reaching values of 2.2 and 2.7 fm respectively for ^{32}S and ^{16}O collisions on Au. This explains why the maxima of the corresponding rapidity distributions in Fig. 12 are not shifted downward to such a degree as to coincide with $y_{cm}(b = 0)$.

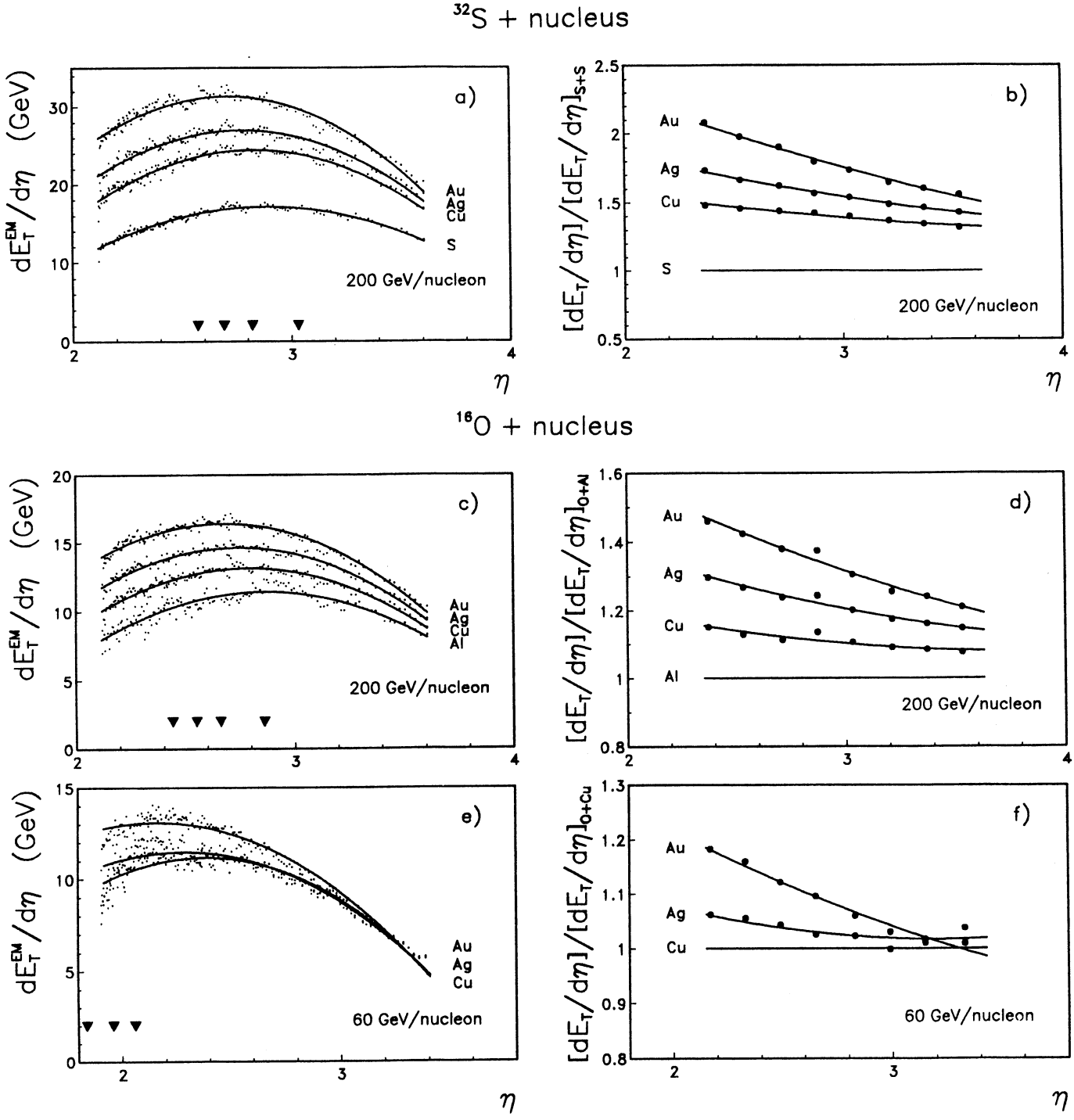

Figure 12 Pseudorapidity distributions for different targets and projectiles for $E_T > E_T^{DI}$. Parts a), b) show $dE_T^{EM}/d\eta$ for S+Au, Ag, Cu, S and $dE_T/d\eta$ relative to S+S. Parts c), d) show $dE_T^{EM}/d\eta$ for O+Au, Ag, Cu, Al at 200 GeV/nucleon and $dE_T/d\eta$ relative to O+Al. Parts e), f) show $dE_T^{EM}/d\eta$ for O+Au, Ag, Cu, at 60 GeV/nucleon and $dE_T/d\eta$ relative to O+Cu. Compare with Fig. 11. In a), c) and e) $\eta = y_{cm}$ values are marked by triangles for $b = 0$ for the corresponding target projectile combinations (see Table 9).

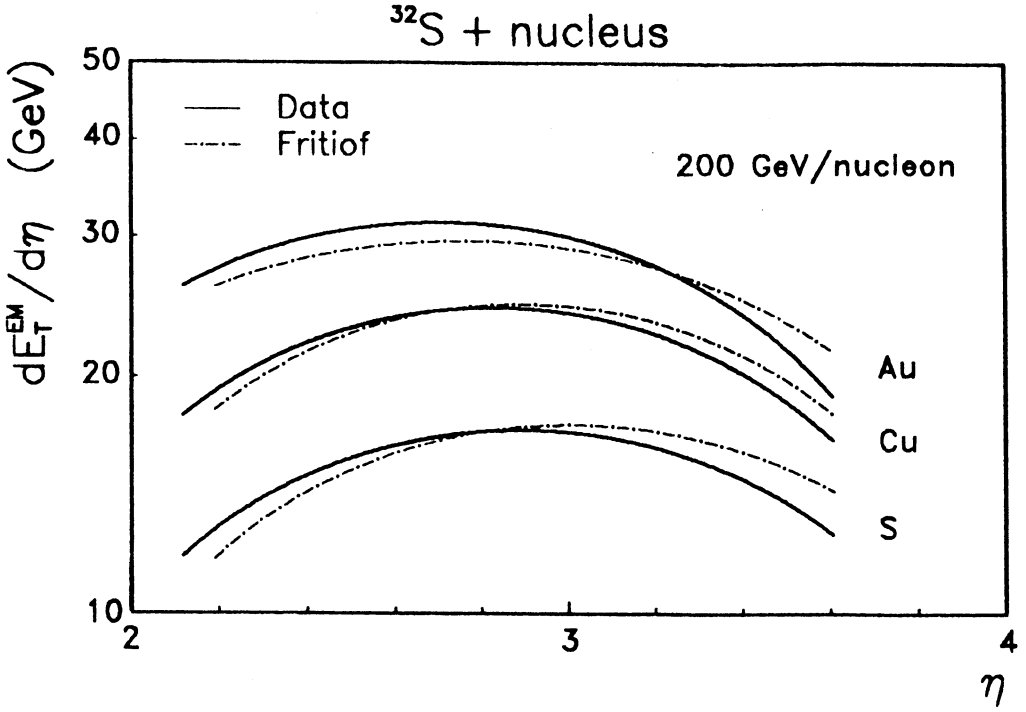

Figure 13 Pseudorapidity distributions for S+Au, Cu and S for data and Fritiof for events with total transverse energy $E_T > E_T^{DI}$ (data) and $E_T > E_T^{NS}$ (Fritiof).

in mind in comparing and analyzing E_T data that refer to a limited η–domain only: the average exponent α depends on the experimental acceptance. Consequently one would prefer to base a simple consideration of E_T systematics on full 4π acceptance results. As our own data refer to a limited acceptance we investigate, by means of a Fritiof extrapolation of the data to 4π, the possible consequences of this limitation.

To extrapolate our E_T data for 'central' collisions (the B0 values of Table 3) to 4π we employ acceptance correction factors obtained from Fritiof. These are given in Table 8, for a $b \cong 0$ Fritiof calculation. Surprisingly, all correction factors are close to the mean value of 2.1, i.e. our acceptance always covers about 48% of the total E_T predicted by Fritiof for head–on collisions, the excursions from this mean value being only on the order of a few percent. Accepting the Fritiof prediction as a semi–empirical correction, we list E_T 'data' in full phase space in Table 8. These data refer to the central (B0) collision points described in section 4.1 and listed in Table 3 for the various systems. Table 8 also gives the 'scaling' factors for S/O projectiles on various targets at 200 GeV, and for the E_T ratios of 60/200 GeV/nucleon (for the oxygen projectile). In comparing these scaling results with the corresponding values inside our acceptance (Tables 4 and 5) we see that all S/O and 60/200 ratios are somewhat reduced here (with the relative trends preserved). However, the overall difference of measured and 4π results is small, reflecting the small degree of variation in the Fritiof 4π correction factors. Thus our acceptance, of $\Delta\eta = 1.7$, is not too asymmetric relative to η_{cm} and appears surprisingly well suited to account for the 4π systematics.

Fig. 14 a shows the systematics of target mass dependence of the total 4π transverse energy for central collisions (Table 8). At 200 GeV/nucleon the data obtained for the oxygen and sulphur projectiles exhibit a similar increase with target mass A, the average ratio of ^{32}S to ^{16}O transverse energies being about 1.8. The total E_T increases approximately as $A^{1/3}$. At 60 GeV/nucleon incident energy the increase with A is significantly flatter.

We turn now to the alternative approach toward an acceptance–independent E_T systematics, by considering the maxima in the rapidity distributions, $dE_T/d\eta$, recorded for central collisions. In preparation for this we first investigate the dependence on centrality (total E_T) of the values $(dE_T/d\eta)_{max}$. Fig. 15 shows $dE_T/d\eta$ at the peak of the η distributions for various, successive intervals of E_T recorded in our acceptance. For both S+Au and O+Au at 200 GeV/nucleon, the peak value of $dE_T/d\eta$ increases somewhat faster than the total E_T. This should be a consequence of the systematic change in the widths of the η distributions, which decrease slightly from peripheral to central collisions, the created transverse energy getting more concentrated near the center of mass rapidity. A similar effect occurs if we proceed toward higher target mass in central collisions induced by a given projectile nucleus (Fig. 12). As a consequence of these observations one expects to obtain a slightly steeper increase of $(dE_T/d\eta)_{max}$ with A in central collisions than the increase observed for the A dependence of the total E_T.

System	$E_T^{4\pi,B0}$ (GeV)	$[E_T^{4\pi}/E_T^{acc}]_{b=0}^{Fritiof}$	$E_T^{4\pi,B0}/E_T^{max}$
200 GeV			
S+Au	360	2.11	0.52
S+Ag	305	2.10	0.49
S+Cu	255	2.11	0.47
S+S	188	2.16	0.43
200 GeV			
O+Au	193	2.15	0.49
O+Ag	167	2.14	0.47
O+Cu	143	2.14	0.45
O+Al	102	2.17	0.39
60 GeV			
O+Au	114	2.08	0.58
O+Ag	104	2.04	0.59
O+Cu	94	2.01	0.59
$(S/O)_{200GeV}$			
Au	1.86	–	1.07
Ag	1.83	–	1.05
Cu	1.79	–	1.04
(O_{60}/O_{200})			
Au	0.59	–	1.20
Ag	0.63	–	1.27
Cu	0.66	–	1.31

Table 8 Transverse energy for central collisions (B0) extrapolated to 4π acceptance ($E_T^{4\pi,B0}$). The ratios $[E_T^{4\pi}/E_T^{acc}]_{b=0}$ (Fritiof) and $E_T^{4\pi,B0}/E_T^{max}$ are also given (for E_T^{max} see Table 9). Sulphur and oxygen values are compared for 200 GeV/nucleon and 60 with 200 GeV/nucleon for oxygen.

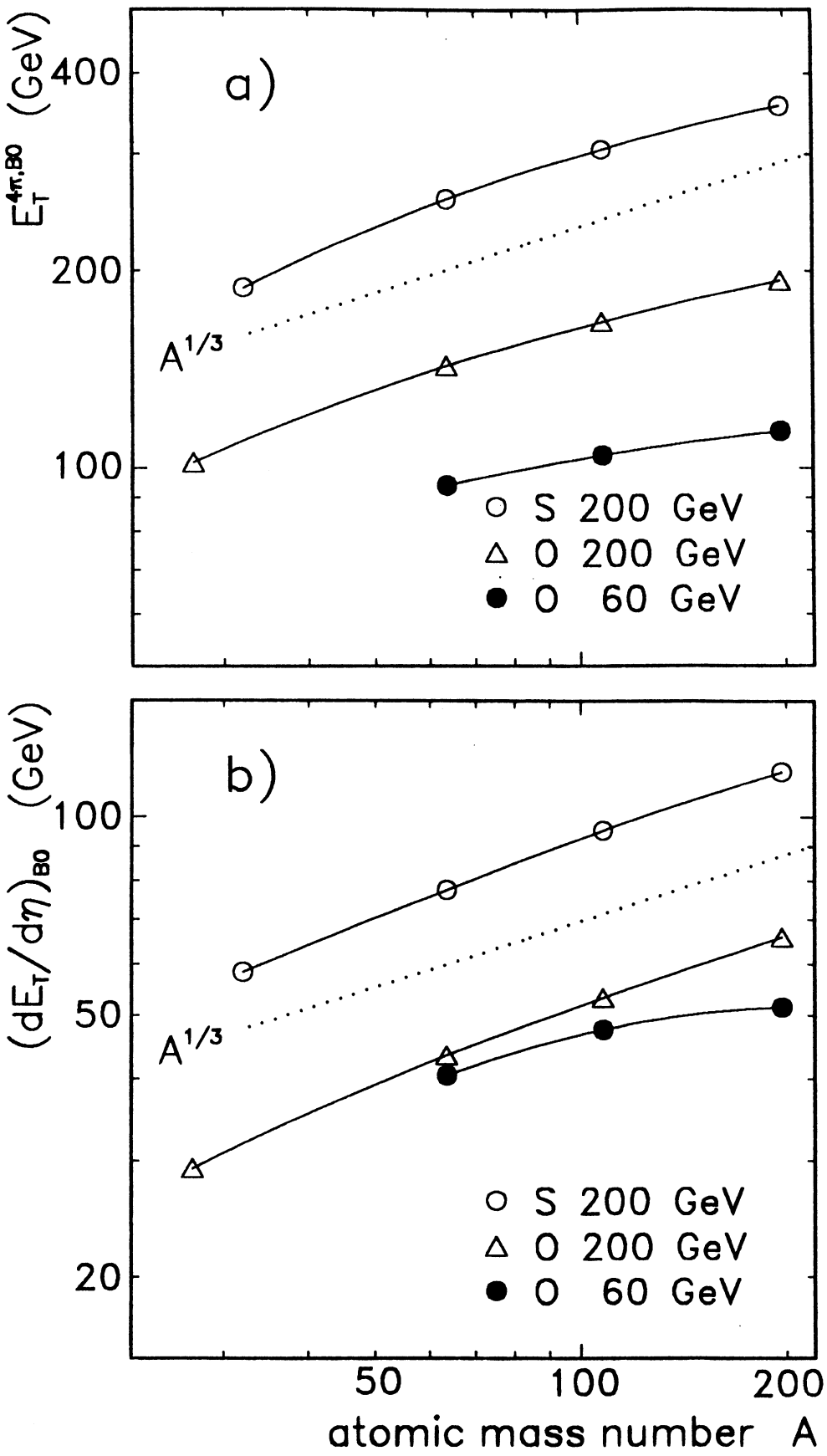

Figure 14 Mean transverse energy for central collisions, extrapolated to 4π, $E_T^{4\pi,B0}$ (a) and pseudorapidity density $dE_T/d\eta$ at $\eta = y_{cm}^{b=0}$ for $E_T = E_T^{B0}$ (b) as a function of the target mass number for S+Au, Ag, Cu, S and for O+Au, Ag, Cu, Al at 200 GeV/nucleon, for O+Au, Ag, Cu at 60 GeV/nucleon. In both cases a $A^{1/3}$ behaviour is indicated by a dotted line.

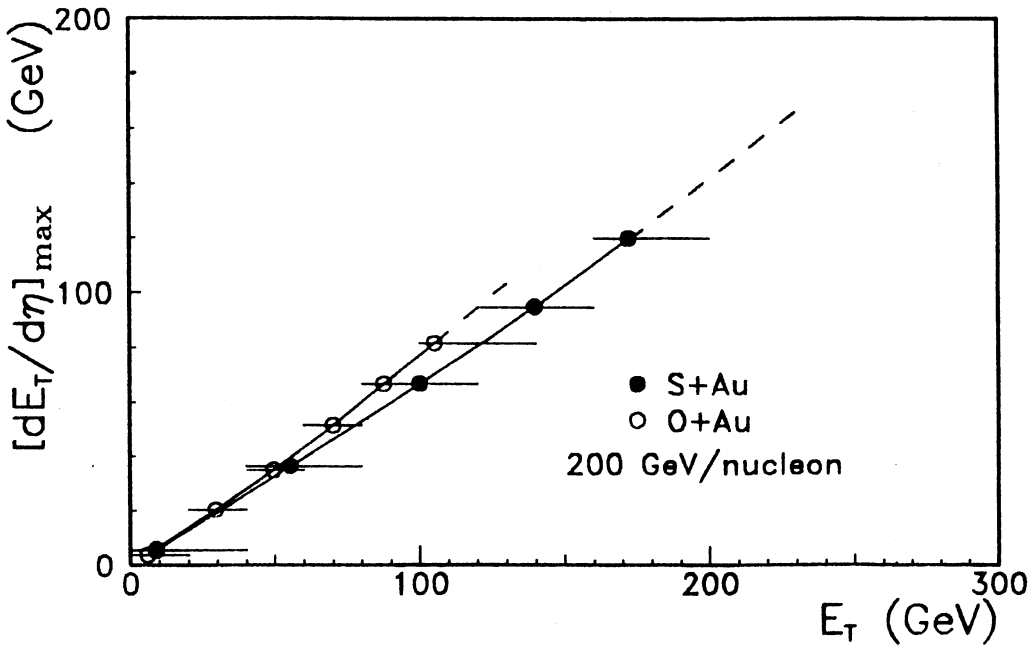

Figure 15 Maximum pseudorapidity density $dE_T/d\eta$ for ^{32}S and ^{16}O on Au at 200 GeV/nucleon as function of the mean E_T in transverse energy bands, indicated by the horizontal error bars. Dashed lines extrapolate the fit (full lines) to E_T values maximally reached for the reactions.

Fig. 14 b gives the systematics of $(dE_T/d\eta)_{B0}$ obtained from the rapidity distributions of transverse energy. For oxygen and sulphur projectiles at 200 GeV/nucleon incident energy we observe an increase with A which is somewhat steeper than the slope of the full acceptance E_T values in Fig. 14 a. Assuming an A^α dependence we obtain an *average* $\alpha = 0.40$ for the O+nucleus and S+nucleus data at 200 GeV/nucleon. The 60 GeV/nucleon data for O+nucleus exhibit a remarkably different behaviour. The increase with A is flatter and non–linear. The flatter rise of the 60 GeV/nucleon data is also seen in the acceptance–integrated E_T values shown in Fig. 14 a but it is close to linear in that case. However, the 60 GeV/nucleon values of $(dE_T/d\eta)_{B0}$ are much closer to the O+nucleus data obtained at 200 GeV/nucleon. For the Cu target they are almost equal, in contrast to the integrated E_T data, where they differ by factors of about 1.5. This aspect of the data is a consequence of the narrower longitudinal phase space at 60 GeV/nucleon, and the correspondingly narrower widths of the rapidity distributions: the peak to integrated E_T ratio is higher at the lower energy.

Summarizing the above observations we note that

1) Experiments investigating the systematics of transverse energy production, observed for light–projectile/heavy–target central collisions in a *finite*, non 4π rapidity interval are confronted with a shift in the rapidity distribution of E_T with increasing target mass, relative to the fixed, finite acceptance. In order to obtain acceptance–independent stopping power systematics one may either extrapolate to 4π, or consider the systematics of $(dE_T/d\eta)_{max}$ values.

2) Both approaches yield similar results concerning the target mass dependence of E_T in central collisions as long as different (light) projectiles are compared at the same incident energy. At 200 GeV/nucleon the target mass dependence of E_T is reasonably well approximated by A^α law, both for oxygen and sulphur projectiles. The parameter α is slightly larger fro the peak values $(dE_T/d\eta)_{B0}$ than for the 4π values of E_T.

3) Investigating, however, the dependence of E_T production on the incident energy for a fixed projectile–target central collision system, the two methods lead to drastically different results. The peak value of $dE_T/d\eta$ increases much more slowly with incident energy than the total E_T yield. This is a consequence of the increasing width of the rapidity distribution.

From comparison of our data to the Lund Fritiof model we conclude that, in general, the shapes of the differential E_T distributions (Figs. 5 and 6) and the pseudorapidity distributions $dE_T/d\eta$ (Fig. 13) are well reproduced. This overall agreement is also observed for the systematic dependence, on target/projectile mass and on the incident energy, of total E_T values recorded for central collisions in the acceptance of our calorimeters.

4.4 Correlations between E_T, E_{Veto} and Impact Parameter

We first consider correlations between E_T and E_{Veto}. As we will see, one can extract information that goes beyond that based on E_T and E_{Veto} spectra only. For not–too–central collisions, E_{Veto} represents the energy of the projectile spectators. In correlations between E_T and E_{Veto} we can thus study how the energy of the projectile participants is converted into transverse energy for different target–projectile combinations and projectile energies. The degree of conversion into E_T depends on the number of successive collisions that a participant encounters and, by this, on collision geometry. As we will see further below in this section, impact parameter b and E_{Veto} are correlated allowing an interpretation of E_{Veto} as a measure of centrality. For S+Au, Ag, Cu at 200 GeV/nucleon Fig. 16 a gives mean E_T values for bins in Veto energy with statistical errors as function of E_{Veto} from the Fritiof model. The experimental data are shown in Fig. 16 b. Vertical bars correspond to statistical errors. We see that for all targets the correlations are very similar down to Veto energies of about half beam energy. We conclude that for peripheral collisions E_T is produced proportionally to the number of interacting projectile nucleons that do not go into the Veto calorimeter, and that this is independent of the size of the target nucleus. For large impact parameters, most projectile participants interact only once, as the projected target nuclear densities are relatively low. The same observation is made at 60 GeV/nucleon for O+Au, Ag and Cu, even down to a smaller fraction of the beam energy reaching the Veto Calorimeter (Figs. 16 e, f).

For lower E_{Veto}, i.e. more central events, multiple interactions of projectile participants occur and the E_T–E_{Veto} correlation exhibits an increase in produced E_T per loss in E_{Veto} (except for the S+S case). Thus at lower E_{Veto} we encounter a gradually stronger target mass dependence if we go to higher centrality. The S+S reaction is an exception in this respect. At low forward energy, experimental as well as Fritiof correlations show less E_T to be produced than expected for a linear E_T–E_{Veto} correlation. An indication of this persists in S+Cu. Recall the lower probability to reach high E_T for smaller targets that was seen already in the E_T spectra (Fig. 5). Thus, in central collisions the energy not going forward is converted into E_T to a higher degree for larger target nuclei, for which we expect an increased probability for a projectile nucleon to interact several times in the target. The first interaction scatters it away from the Veto Calorimeter. The more interactions follow, the more E_T will be produced for the same missing forward energy.

The overall agreement of Fritiof predictions with the data also extends to the fluctuation in E_T–E_{Veto} correlations. This is illustrated for the O+Au reaction in Figs. 16 c, d. Vertical bars indicate $\pm$ 1 rms for Fritiof and experimental data to demonstrate that the width of the correlation is also reproduced well by the model.

For non–central events the amount of produced E_T per projectile participant is quite independent of the size of the non participating part of the projectile. This can be seen from a comparison between S+Au and O+Au E_T–E_{Veto} correlations. They agree for E_{Veto} higher than half the beam

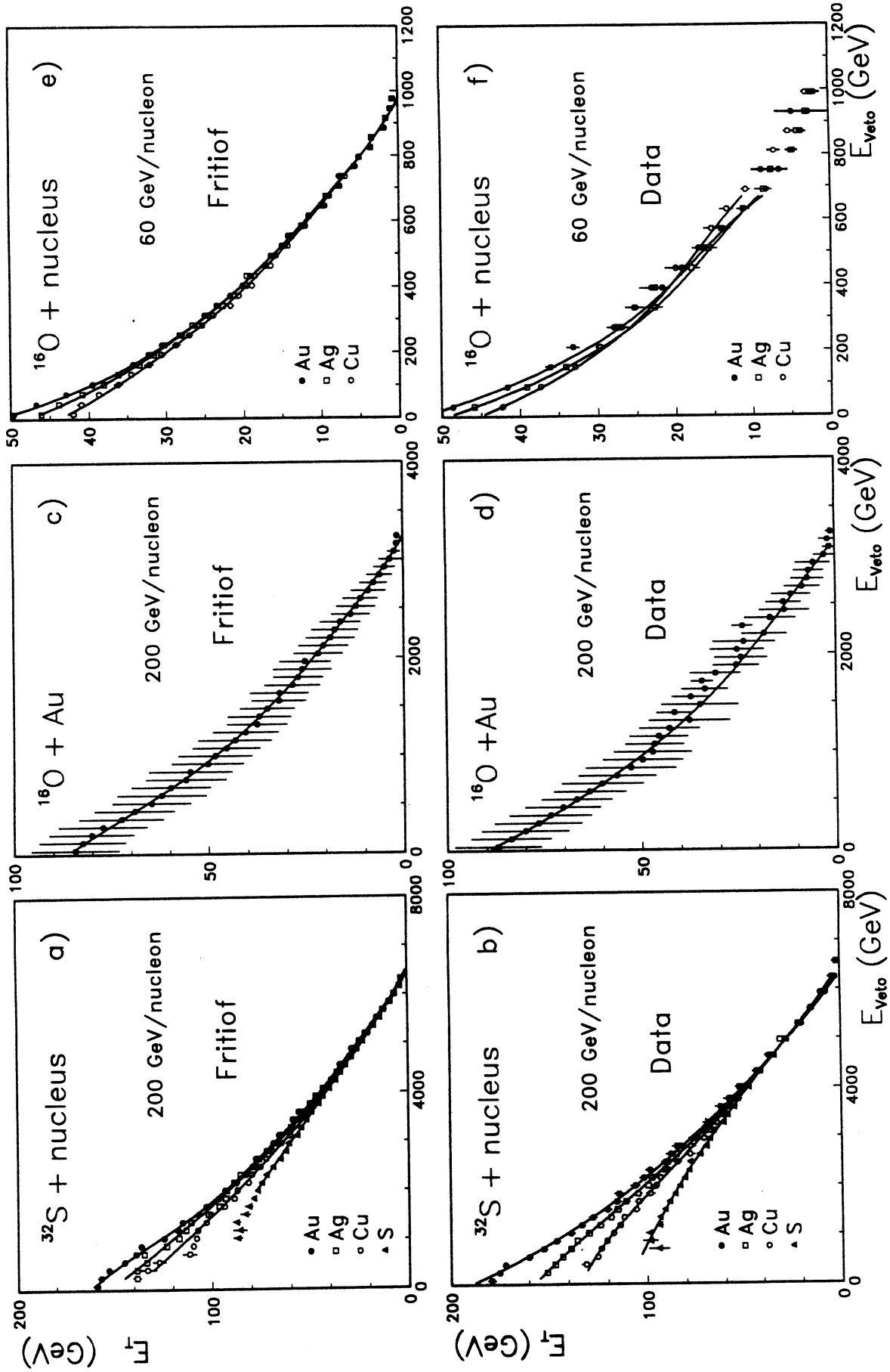

Figure 16 Correlation between transverse energy, E_T, and forward energy flux, E_{Veto}. In a) and b) mean E_T values are plotted as function of E_{Veto} for Fritiof and experimental Data for S+Au, Ag, Cu, S at 200 GeV/nucleon with fits given as full lines. e), f) show equivalent correlations for O+Au, Ag, Cu at 60 GeV/nucleon. In c) d) rms values for each bin are given additionally as vertical bars for O+Au at 200 GeV/nucleon.

energy, as seen in Figs. 16 b and d. We may note that a similar agreement is observed in a comparison with correlations for 60 GeV/nucleon if E_T is scaled by the available cm energy (ratio 0.5 between 60 and 200 GeV/nucleon), as was done in Figs. 16 e, f.

The impact parameter b defines the collision geometry. Unfortunately, it is not a directly measurable observable. As E_T and E_{Veto} spectra and the correlations between these quantities are reproduced well by Fritiof we investigate next how E_T and E_{Veto} are correlated to b, for the different projectile–target combinations. For O+Au collisions at 200 GeV/nucleon Figs. 17 a and b show how E_T and E_{Veto} are correlated with impact parameter b, in Fritiof. In c and d the mean impact parameter and its rms are given as functions of E_T and E_{Veto}. Neither the correlation of b with E_T nor that with E_{Veto} exhibit linearity over the full range. We see that impact parameters smaller than about 2 fm can not be significantly enhanced by choosing extremely high E_T, or extremely low E_{Veto} values.

From our model calculation with homogeneous spheres (Table 7) we get b_{DI}=4.08 fm for complete dive–in and b_{total}=10.32 fm for grazing collisions of O+Au. These values are indicated in Fig. 16 . We also indicate $< b >_{DI} = 2/3 \cdot b_{DI}$ at 2.72 fm. Thus, it is possible to select for impact parameters slightly smaller than the average value for complete dive–in by setting thresholds (triggering) on E_T or E_{Veto}. Zero impact parameter, of course, can not be selected by any trigger.

To see whether the same is true for other projectile–target systems consider Fig. 18. Parts a, b and c give mean impact parameters as a function of E_T, and d, e, f as a function of E_{Veto}. Indicated by horizontal dotted lines are $< b >_{DI}$ values for Au, Ag and Cu targets (see Table 7). We find a confirmation of our conclusion that a selection of impact parameters much smaller than $< b >_{DI}=2/3 \cdot b_{DI}$ is hardly possible with E_T or E_{Veto}. For 60 GeV/nucleon a selection by E_{Veto} is less effective than at 200 GeV/nucleon and less so than a selection by demanding high E_T. These findings may be specific to our Veto Calorimeter acceptance. Selection efficiency by E_T is equally good for 60 and 200 GeV/nucleon oxygen projectiles. To select a sample with the smallest impact parameters from the data we could simultaneously demand highest E_T and lowest E_{Veto}, but $< b >$ values considerably lower than $3/4 \cdot < b >_{DI}$ are hardly enhanced.

5 Stopping Power and Energy Density

5.1 Stopping Power Systematics

In chapter 4.3 we have gathered systematic data concerning the production of transverse energy in central collisions. The dependence both on the projectile and target nuclei, and on the incident energy was investigated. The discussion of nuclear stopping power is based on a comparison of the created transverse energy to the total available center of mass energy. The latter is obtained from the projectile incident energy, and from the number of participating nucleons of the target.

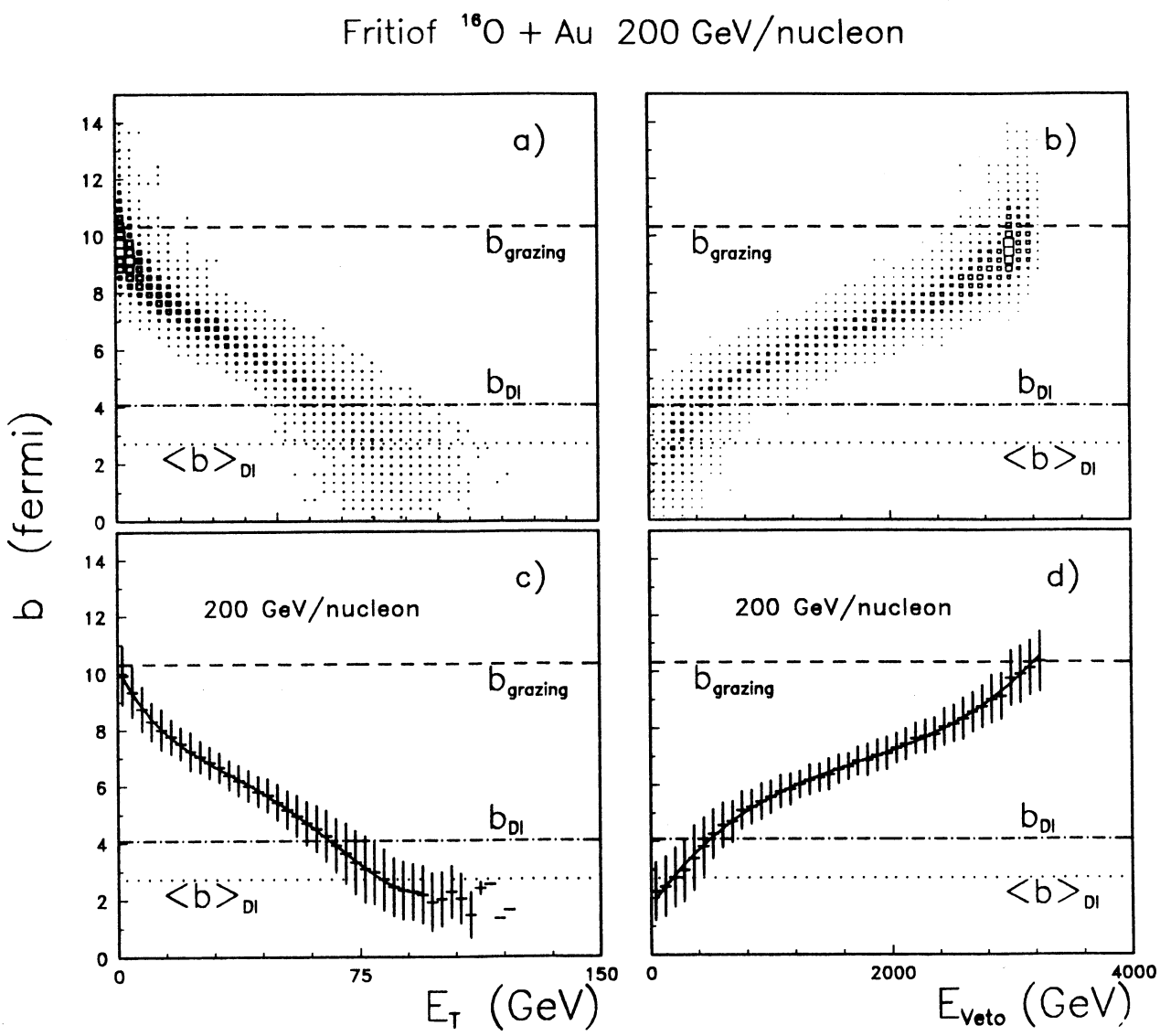

Figure 17 Fritiof simulation for O+Au 200 GeV/nucleon: correlations between a) impact parameter b and E_T, and b) b and E_{Veto} as scatter plots and correspondingly in c), d) mean b values in bins of E_T and E_{Veto} with $\pm$ 1 rms indicated as vertical bars. Impact parameters for grazing collisions are given by dashed horizontal lines, for DI as dash-dotted and mean impact parameters for DI as dotted lines.

We employ a simple model for the reaction kinematics, in identifying our E_T data for near–central collisions with zero impact parameter collisions, and evaluating the participant nucleon numbers from a clean–cut geometry of intersecting homogeneous spheres. For head–on collisions of a projectile with nucleon number B with a target with A nucleons, the number of participants is $n_{part}^{total} = n_{part}^{projectile} + n_{part}^{target}$. In a light–projectile/heavy–target collision the number of projectile participants is B, and

$$n_{part}^{target} = A - B[(A/B)^{2/3} - 1]^{3/2}. \qquad (1)$$

The participant numbers for zero impact parameter collisions of oxygen and sulphur with various targets are given in Table 9, along with the corresponding values of $\sqrt{s}$ and the center of mass rapidity y_{cm}.

The energy E_{cal} that can be seen by calorimetry is $E_{cal}=\sqrt{s}-m_{part}$ where m_{part} is the total rest mass of the participating nucleons. The transverse fraction of the observable energy depends on the momentum distribution. For an isotropic distribution $E_T = (\pi/4) \cdot E_{cal}$, and the corresponding E_T seen in a 4π calorimeter is $E_T^{max} = (\pi/4) \cdot (\sqrt{s} - m_{part})$. This transverse energy has been labelled 'maximal' because, in general, the longitudinal phase space is more extended than the transverse one, thus reducing the transverse fraction of the total energy. The values of E_T^{max} and E_T^{max} per participant are given in Table 9. The dependence of participant numbers, and of E_T^{max} on the target mass A is illustrated in Fig. 19. E_T^{max} increases close to the indicated $A^{0.2}$ dependence, and E_T^{max}(60 GeV)=0.5 E_T^{max}(200 GeV).

Accepting E_T^{max} as the natural scale relative to which the observed E_T should be evaluated, we list in Table 8 the ratios $E_T^{4\pi,B0}/E_T^{max}$ where $E_T^{4\pi,B0}$ represents the near–zero impact parameter (B0) values of E_T, extrapolated to full 4π acceptance with the Fritiof model. At 200 GeV/nucleon incident energy, for the sulphur projectiles the observed fraction of E_T^{max} increases from about 0.42 to 0.52 in going from light to heavy target nuclei. We interpret this trend (observed for both projectile nuclei) as a rise in nuclear stopping power. This conclusion is also obtained from a comparison of the increase with A of $E_T^{4\pi,B0}$, given in Fig. 14, and from the dependence of E_T^{max} on A shown in Fig. 19. The parametrization of the form A^{α} yields an average $\alpha = 0.34$ in the former, and $\alpha = 0.23$ in the latter case. The ratio $E_T^{4\pi,B0}/E_T^{max}$, which we identify as the *relative* nuclear stopping power, thus increases with A^{α} but only very slowly, α being 0.11 ± 0.04 at 200 GeV/nucleon incident energy. At 60 GeV/nucleon, on the other hand, we find *no* increase of the $E_T^{4\pi,B0}/E_T^{max}$ ratio (Table 8), i.e. a constant relative stopping power. However, the observed value, of about 0.6, is *higher* than at 200 GeV/nucleon (where it ranges from 0.4 to 0.5). These results are consistent with the results of WA80 [17]. The experiment BNL–E802 obtained data at 14.5 GeV/nucleon for oxygen and silicon projectiles [18]. At this, yet lower energy, the relative stopping power was found to stay constant above A=64 (Cu).

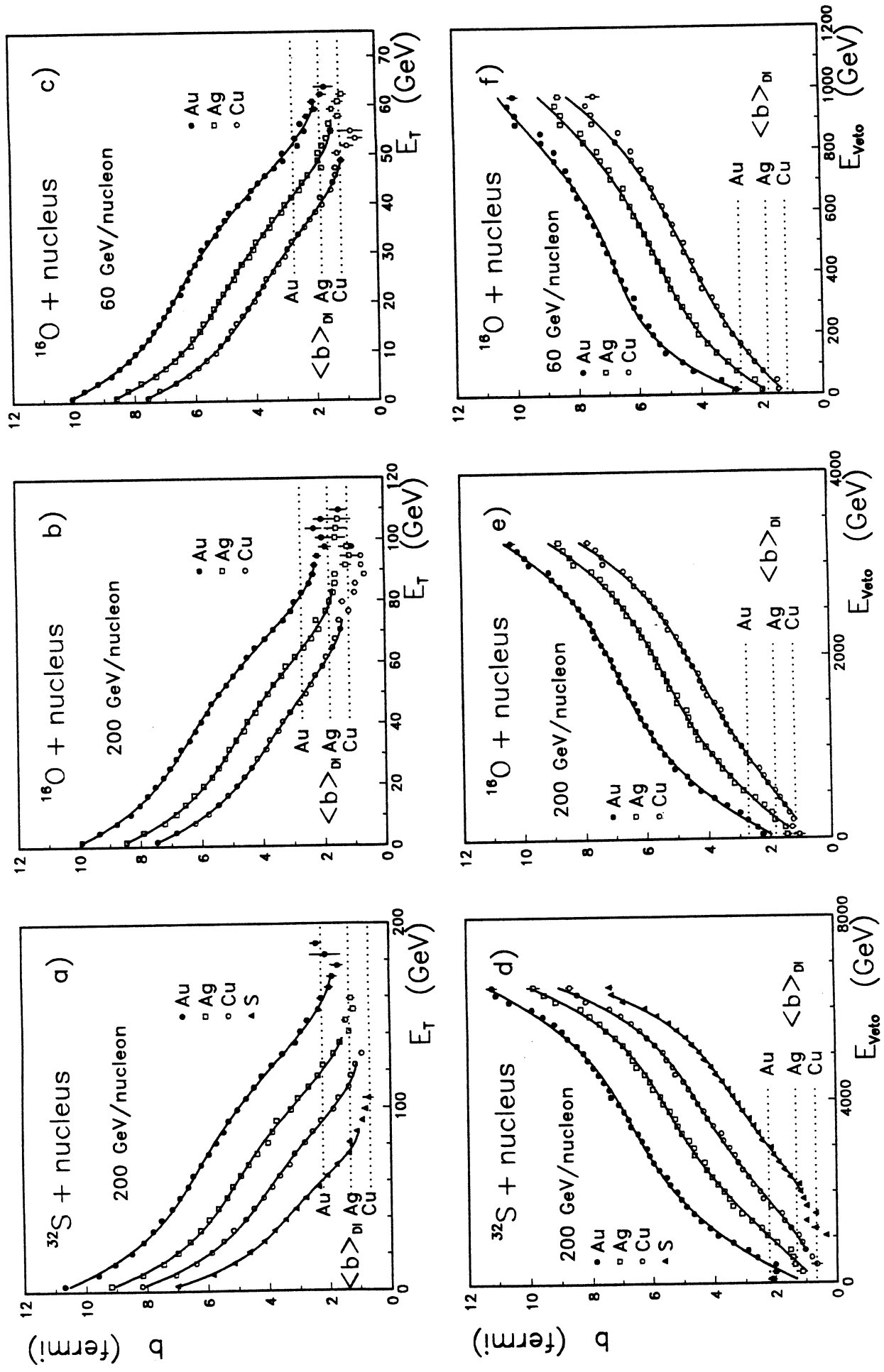

Figure 18 Fritiof generated correlations between E_T, E_{Veto} and impact parameter b for S+Au, Ag, Cu at 200 GeV/nucleon (a, d) and O+Au, Ag, Cu at 200GeV/nucleon (b, e) and at 60 GeV/nucleon (c, f). Mean values are given with statistical errors together with fits to guide the eye. $< b >_{DI} = 2/3 \cdot b_{DI}$ is indicated as dotted horizontal lines for Au, Ag and Cu as targets.

System	n_{part}^{target}	n_{part}^{total}	y_{cm}	$\sqrt{s}$ (GeV)	E_T^{max} (GeV)	E_T^{max}/part (GeV)
200 GeV						
S+Au	81	113	2.57	990	695	6.1
S+Ag	63	95	2.69	875	617	6.5
S+Cu	50	82	2.81	774	548	6.7
S+S	32	64	3.03	622	441	6.9
200 GeV						
O+Au	53	69	2.44	565	393	5.7
O+Ag	42	58	2.55	504	353	6.1
O+Cu	34	50	2.65	454	319	6.4
O+Al	23	39	2.86	370	262	6.8
60 GeV						
O+Au	53	69	1.84	313	195	2.8
O+Ag	42	58	1.95	278	176	3.0
O+Cu	34	50	2.06	250	160	3.1

Table 9 Number of participants and kinematical parameters for sulphur and oxygen induced interactions for b=0.

System	$dE_T/d\eta(\eta = y_{cm})$	ϵ_{Bj}
S+Au	117	2.6
S+Ag	95.3	2.1
S+Cu	77.6	1.7
S+S	58.3	1.3
200 GeV		
O+Au	65.8	2.3
O+Ag	53.2	1.9
O+Cu	43.4	1.5
O+Al	29.2	1.0

Table 10 $dE_T/d\eta$ at $\eta = y_{cm}$ extrapolated to E_T^{B0} and the energy density values according to the Bjorken model (see text).

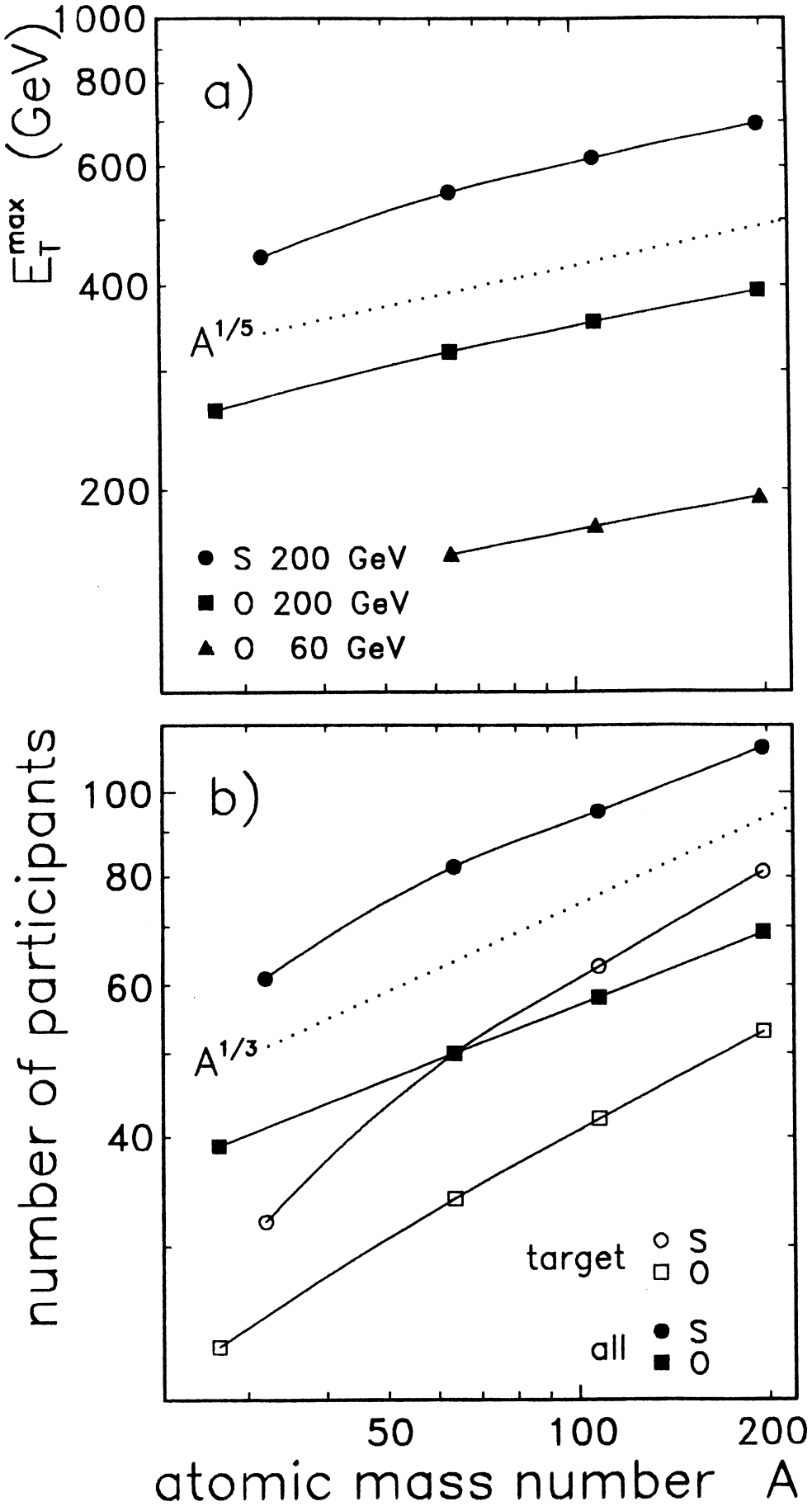

Figure 19 a) Maximum observable transverse energy, E_T^{max}, for full 4π acceptance as a function of the target mass number A for ^{16}O+nucleus at 60 GeV/nucleon and 200 GeV/nucleon, and ^{32}S+nucleus at 200 GeV/nucleon (for homogeneous spheres and $b = 0$). b) Number of participants (filled symbols) and number of target participants (open symbols) for central collisions ($b = 0$) for ^{32}S+nucleus and ^{16}O + nucleus as a function of A (see Table 9).

We have limited the discussion above to the E_T values observed at the 'characteristic point' for central collisions (B0 in Table 3). The identification of the B0 (central collision) points along the differential E_T distributions was, in itself, not completely free of model assumptions. So, for a final overall consideration we return to the full differential E_T spectra of Fig. 4 which we replot in Fig. 20 on a scale $X = E_T^{4\pi}/E_T^{max}$, after extrapolating the experimental E_T values to 4π acceptance using the Fritiof acceptance correction factors listed in Table 8. In this re–scaled version we show all our data, for both projectile nuclei and at both energies. The figure also indicates the 'B0' characteristic points (asterisks). After rescaling to E_T^{max} the B0 values represent the relative stopping power ratios $E_T^{4\pi}/E_T^{max}$, discussed above. They increase with target A, for oxygen– and sulphur–induced reactions at 200 GeV/nucleon and stay constant at 60 GeV/nucleon, but at a higher value.

Considering the tail regions of the X–distributions, beyond the B0 points, we observe a simple overall behaviour: all X–distributions converge toward each other. In other words: each (central) collision system, at fixed incident energy and projectile nucleus reaches its appropriate 'maximum' E_T at nearly the same (low) cross section. This is clear in the O+nucleus data at 60 GeV/nucleon where our data extend to almost $X = 1$, at a cross section level which is more than 4 orders of magnitude below the central collision (B0) cross section (i.e. in the μbarn–domain). If the trend, seen with decreasing cross sections, continues beyond $X = 1$ one would even expect a cross–over of the curves for the three target nuclei, the Cu–data coming up to the top. At 200 GeV/nucleon the data for the oxygen projectile reach $X \approx 0.7$ at 100 μbarn cross section which marks the limit of our statistics. A qualitatively similar convergence of the curves is seen here. Turning, finally, to the S+nucleus data at 200 GeV/nucleon, convergence is not yet reached at $X \approx 0.65$, the end of our coverage.

We make two observations: one is the increase of the E_T tail slope in going from O+Au to S+Au at 200 GeV/nucleon. The other is a steeper slope of the O+Au transverse energy distribution tail in comparison to the O+Cu data, an effect visible both at 60 and 200 GeV/nucleon. Both trends point toward a statistical interpretation of the E_T tail cross sections. Fluctuations at the level of the individual participant nucleons (e.g. their rescattering variation, or the transverse energy fluctuation in participant nucleon–nucleon collisions) should allow to reach larger X more readily the smaller the average number of participant nucleons is. We have previously invoked the same argument in section 4.1.

A further source of fluctuations, not envisaged in our naive geometrical model, could be a fluctuation of the target participant number. This effectively changes E_T^{max} in collisions where n_{target} exceeds the prediction of a clean cut geometry. Clearly, the relative fluctuation width of n is higher in systems with a smaller number of participants. We therefore expect this effect to be most prominent in proton–nucleus collisions. In fact, the tail slope of the E_T distributions is

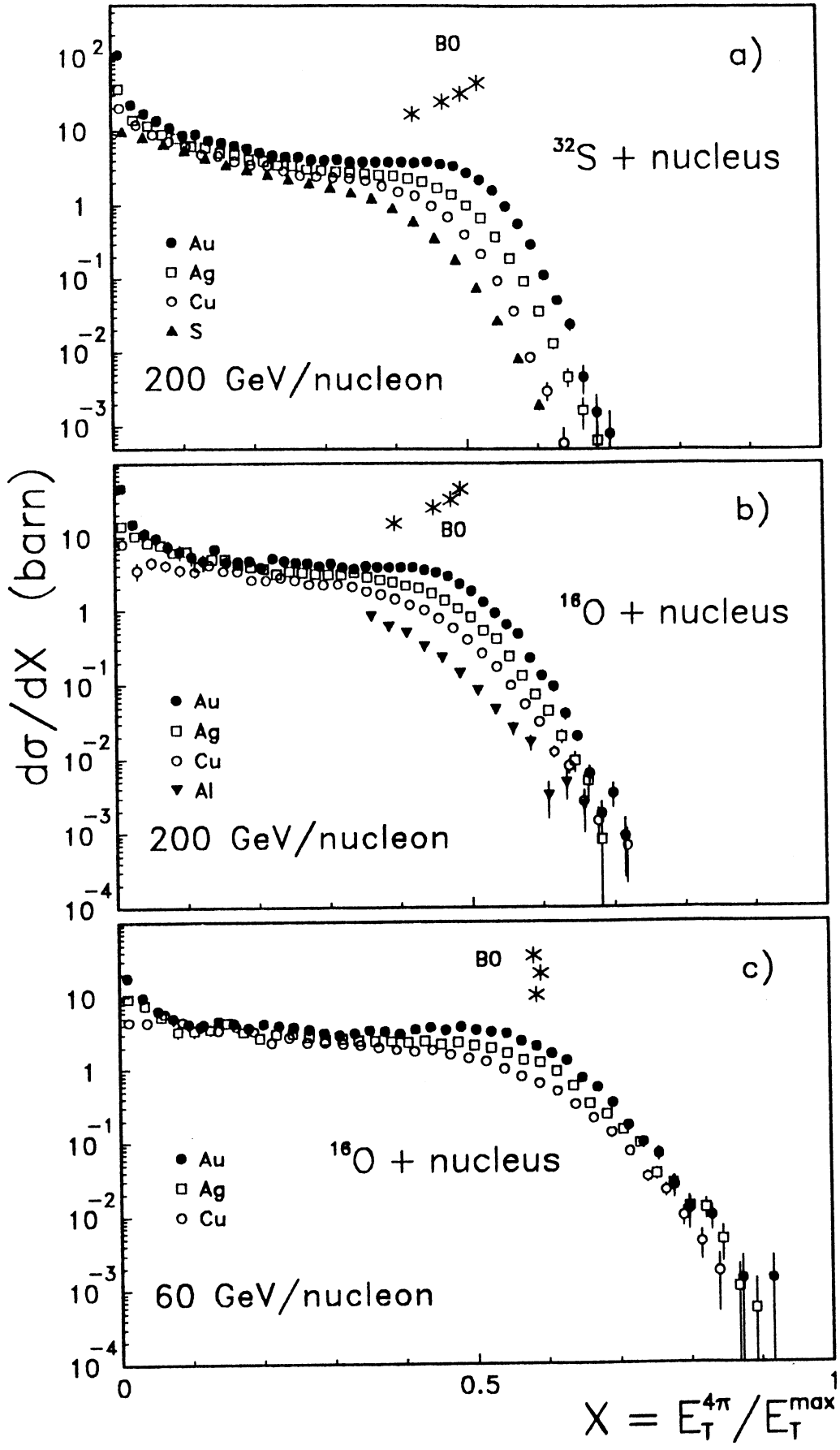

Figure 20 Transverse energy spectra extrapolated to 4π acceptance and scaled with E_T^{max} (see Tables 8 and 9) at 200 GeV/nucleon a) for ^{32}S+Au, Ag, Cu, S and b) for ^{16}O+Au, Ag, Cu, Al. c) Scaled spectra at 60 GeV/nucleon for ^{16}O+Au, Ag, Cu. Marked with asterisk are equivalently scaled E_T^{B0} values. E_T^{max} for b=0 was used.

far flatter for p+nucleus (see section 6) than in O+nucleus or S+nucleus collisions at the same energy. Finally, E_T fluctuations into our finite acceptance window can influence the shape of the high E_T tail of the E_T distributions. The average correction factor that we employed in the E_T extrapolation to 4π may thus be inappropriate for some of the tail events. We make no attempt here to disentangle the various types of fluctuations that govern the region of extremely high E_T events. Among the fluctuations considered, only the former effects (i.e. increased inelasticity at the microscopic hadron–hadron rescattering level) lead to a genuine increase in the *relative* stopping as measured by the X variable, beyond the central collision average. The latter two effects lead to an overestimate of $X = E_T^{4\pi}/E_T^{max}$ in our procedure because $E_T^{4\pi}$ might be overestimated (by fluctuation into the acceptance window) and E_T^{max} underestimated (more target participant nucleons than given by equation (1)) for certain rare events. The question whether 'full stopping' is indeed closely approached within the data presented here can thus not be conclusively answered. However, irrespective of the degree of stopping, prevailing in the tail events, we may still consider such events interesting because of their high energy density at or near midrapidity. We turn to this aspect in the next section.

5.2 Energy Density

We have shown in the previous section that the relative stopping power at 200 GeV/nucleon may be as high as 50% in central collisions on heavy targets. Thus the available c.m. energy of the SPS gets efficiently utilized, already in *average* central events that occur at cross section levels of some hundred millibarns. The lower limit of cross section at which a calorimeter–triggered tracking detector system can collect sufficient statistics should be reached at the μbarn level. We saw in section 5.1 that S+Au collisions at top SPS energy reach a relative stopping power of about 70% at this cross section level. At lower energies (60 GeV/nucleon) one reaches 100% stopping at such cross section levels, but the *absolute* magnitude of created transverse energy is lower, nevertheless, because of the decrease in the kinematical limits, by a factor of two, in going down from 200 to 60 GeV/nucleon. Therefore, we concentrate on the 200 GeV/nucleon data.

The essential physics at top SPS energy thus may be extracted from event ensembles ranging from 'average central' events with a cross section of several 100 mbarn down to 'high E_T tail' events, at the μbarn level. The stopped fraction of the incident energy increases by only about 40% over this wide range of cross sections. We chose those two event ensembles for an estimate of the energy density in the primordial interaction volume. This energy density is of interest in view of the 'critical' energy density, $\varepsilon \approx 2.5$ GeV/fm^3, ascribed in lattice QCD theory to the hadron→quark–gluon phase transition [19]. Previous investigations of central nucleus–nucleus collisions have shown [2] that energy densities of the required magnitude may be reached, in an extended volume. However the determination of the primordial interaction volume in which the

finally observed transverse energy was concentrated immediately after interpenetration of the two participating nuclear density distributions, remains model–dependent. One normally employs the Bjorken estimate [20] for the energy density,

$$\varepsilon_{Bj} = \frac{(dE_T/d\eta)_{max}}{\pi R^2_{proj} \tau} \qquad (2)$$

where $dE_T/d\eta$ denotes either the E_T per unit of pseudorapidity at the maximum of the $dE_T/d\eta$ distribution or the average $dE_T/d\eta$ observed in the interval $\eta_{cm} \pm 0.5$. These two prescriptions agree if the rapidity distribution is broad, or even flat, i.e. at high incident energy. This is not yet strictly true at 200 GeV/nucleon (c.f. Fig. 12). The maximum value of $dE_T/d\eta$ is about 10% higher than the average $dE_T/d\eta$ in a $\Delta\eta = 1$ interval about the peak of the pseudorapidity distribution. We disregard this difference, basing our consideration on the peak $dE_T/d\eta$ values. The Bjorken estimate for the energy density should not be employed where the difference is large as it is derived for conditions of longitudinal boost invariance (flat rapidity distributions).

In the denominator of equation (2), R is the radius of the projectile nucleus and τ denotes the formation time of the interaction volume, which we interpret as the interpenetration time of the Lorentz–contracted target/projectile discs. At 200 GeV/nucleon incident energy, the Lorentz factor γ is of the order of 10 in the c.m. frame. A plausible choice for τ is 1 fm, a value also adopted in most of the previous analysis of energy density systematics. We note, however, that this choice can not be appropriate at lower energies.

We list in Table 10 the peak values of the $dE_T/d\eta$ distributions, at 200 GeV/nucleon incident energy. These values were obtained by extrapolation (like in Fig. 15) to the central collision (B0) points for each projectile/target combination (Table 3). The energy densities obtained from equation (2) are also shown in Table 10. For the projectile radii we employed $R(^{16}O) = 3$ fm and $R(^{32}S) = 3.8$ fm. The highest energy density is reached in central S+Au collisions ($\varepsilon_{Bj} =$ 2.6 GeV/fm^3) but the corresponding value obtained for O+Au collisions ($\varepsilon_{Bj} = 2.3$ GeV/fm^3) is not much lower. Thus, the difference in the two systems consists mostly in the larger interaction volume of the former. For the lightest targets the energy density falls down to about one–half of the values observed for the Au target.

In order, finally, to give an estimate of the densities reached in events that fall in the tail region of the differential E_T distribution, we again consult Fig. 20. We limit our consideration to the systems O+Au and S+Au at 200 GeV/nucleon, noting again that the high E_T cross sections fall down more steeply in the latter reaction. Two approaches may then be adopted, by evaluating the transverse energy either at the point where the cross sections have dropped down by four orders of magnitude from the B0 (central collision) points indicated in Fig. 20. Alternatively one may consider the E_T values reached at a fixed relative stopping power, for example at $X = E_T^{4\pi}/E_T^{max}$ $= 0.7$. The results of the two extrapolation procedures agree closely, for both reactions. We obtain

energy densities, in the tails of the E_T distributions, of ε_{Bj} = 3.6 GeV/fm^3 for S+Au and ε_{Bj} = 3.4 GeV/fm^3 for O+Au. They reach or, in fact, surpass the critical energy densities expected for the deconfinement transition in lattice QCD. Note, however, that such model calculations refer to a state of zero net–baryon number density whereas the present data correspond to a finite net–baryon density[2].

6 Nucleus–nucleus E_T spectra as a superposition (convolution) of proton–nucleus distributions.

Event simulators for nucleus–nucleus collisions like Fritiof or Venus [21] have in common that, in first order, they assume a superposition of nucleon–nucleon interactions, similar to less refined models like the Wounded–Nucleon Model (WNM) that has been extensively discussed in the literature [23]. The WNM tries to 'explain' nucleus–nucleus results starting from nucleon–nucleon interactions with book–keeping on the number of participating ('wounded') nucleons [10]. Instead of going the long way from nucleon–nucleon to nucleus–nucleus, one can first ask the simpler question of how a superposition of nucleon–nucleus collisions represents what we find in the nucleus–nucleus case, for example the E_T spectra. For that purpose we will start from proton–nucleus spectra and convolute them with weights corresponding to the probabilities given by the impact parameter b for given projectile–target combinations.

Transverse energy spectra for proton–nucleus collisions have been reported by other experiments [3]. For comparison with our nucleus–nucleus data we will use spectra that we have measured in the same acceptances for proton projectiles with our set of calorimeters. For protons, spectral shapes differ significantly from the nuclear case as there is no variation in the number of projectile participants with impact parameter. E_T spectra for proton projectiles on S, Ag and Au targets are shown in Fig. 21 a.

We have previously observed that central O+Au collisions could be described by a 16–fold convolution of non–peripheral p+Au collisions [2]. This conclusion is not affected by the corrections introduced in the course of the present data analysis, since both the proton–nucleus and nucleus–nucleus spectra have been rescaled with almost the same factor. The p+Au spectrum of Fig. 21 b, taken with a Veto trigger in order to reject peripheral interactions, is fitted by the function

$$f(E_T) = const \cdot (bE_T)^{p-1} e^{-bE_T} \qquad (3)$$

also shown in Fig. 21 b. The fit function is then convoluted 32 times. The result is compared to our S+Au data in Fig. 21 d. The corresponding integrated cross sections are weighted with

[2]Calculations based on a modified Fritiof model (SPACER [22]) indicate maximum energy densities of approximately half of ε_{Bj}.

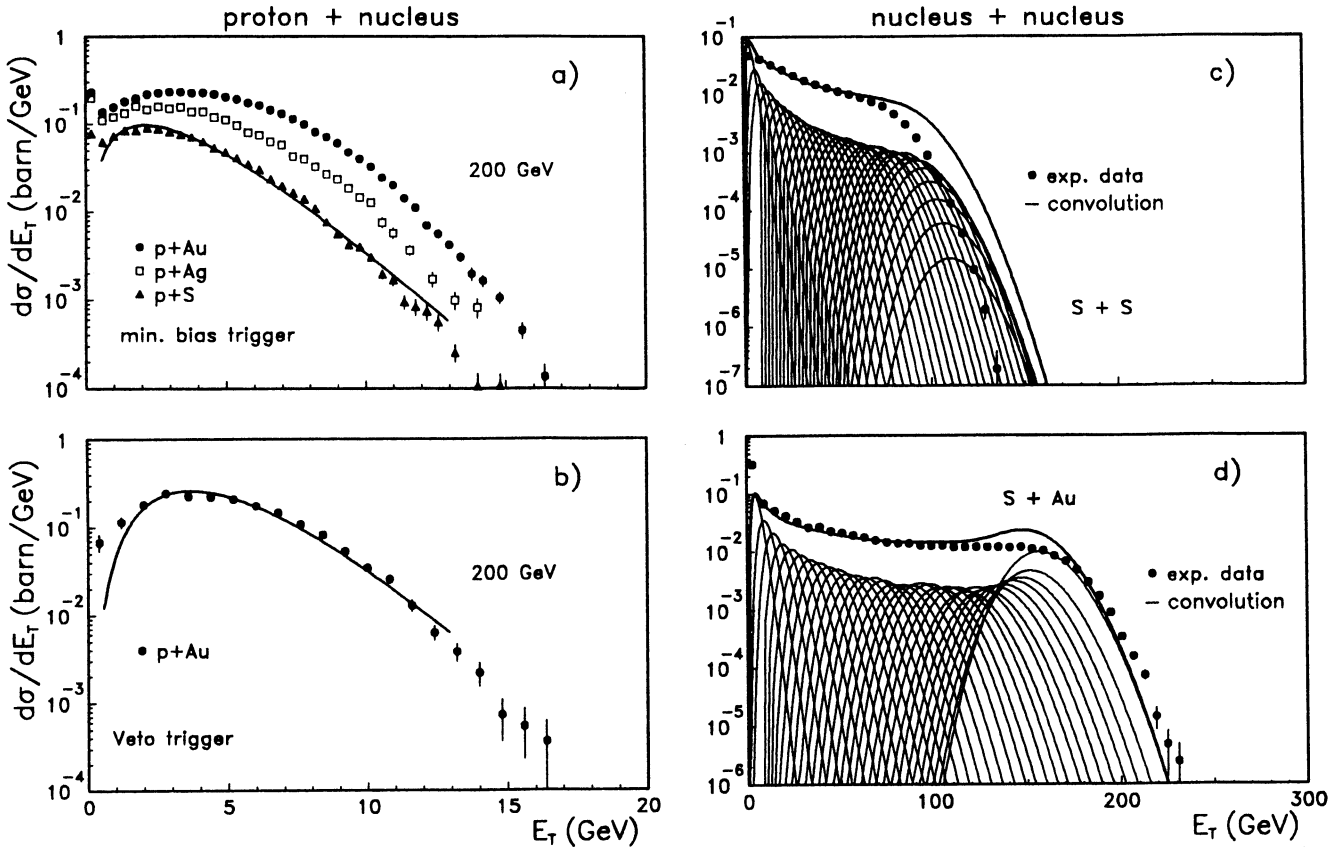

Figure 21 Transverse energy spectra, $d\sigma/dE_T$, a) for p+Au, Ag and S at 200 GeV as seen in identical acceptance as for ^{16}O and ^{32}S projectiles. The solid line is a fit to the sulphur data with the function described in the text. b) p + Au data taken with a Veto calorimeter trigger together with a fit with the same function as above. Spectra for S+S (d) and S+Au (d) at 200 GeV/nucleon in comparison with a sum of n–fold (n=1,...,32) convolutions of the parametrization function derived from a), b) with the probability distribution of n extracted from a simulation based on Fritiof.

proper geometrical probabilities for having n projectile nucleons participating in the interaction. The shape as well as the absolute E_T scale of the spectra are rather well reproduced. The tail cross sections drop somewhat faster than the experimental distribution. This convolution method is valid for asymmetric systems, i.e. light projectiles on heavy targets, since it treats asymmetrically the projectile and target nucleons. In the case of a symmetric system, like S+S, one expects it to be less accurate and indeed this is the case as seen in Fig. 21 c. The convolution of the minimum bias p+S spectrum (Fig. 21 a) over–predicts the S+S data by 20% but the spectral shape comes very close.

7 Conclusions

Although calorimeters are not the instrument with which one can look event by event for the predicted striking signatures of quark matter formation, they are very useful to measure the energy flow in different regions of pseudorapidity and thereby classify the violence of the interaction. The systematic study of sulphur– and oxygen–induced reactions on targets from Al to Au at 200 and 60 GeV/nucleon has shown that the distribution of transverse energy produced in the region $2 < \eta < 4$ reflects very closely the geometry of the colliding nuclei. This was demonstrated in detail by comparison with Monte Carlo (Fritiof) simulations that describe the geometrical aspect of the interactions. The general agreement of such simulations with data is good. This underlines the validity of the picture of an incoherent overlay of nucleon–nucleon collisions that is inherent in most of the Monte Carlo of the interactions. Also a simple convolution of proton–nucleus data with probabilities according to the size of projectile and target comes already quite close in describing the nucleus–nucleus E_T spectra.

A Study of $dE_T/d\eta$ leads to the conclusion that the fraction of the maximum kinematically available transverse energy that is actually observed in central collisions increases from about 40% in S+S, to about 50% in S+Au collisions at 200 GeV/nucleon. The relative stopping power thus increases with A, however very slowly.

At 60 GeV/nucleon we observe a higher relative stopping power, of about 60%, in agreement with previous investigations. We also observe that E_T/E_T^{max} ratios stay constant from O+Cu to O+Au.

We finally employ the Bjorken formula to estimate the energy density, obtaining about 2.5 GeV/fm^3 for average 'central' collisions of both the oxygen and sulphur projectiles with Au target nuclei. For high E_T events, found in the tails of the differential E_T distributions (at, or below the μbarn level of cross sections), we obtain energy densities of about 3.6 GeV/fm^3 at an incident energy of 200 GeV/nucleon. Such an energy density should thus be fully sufficient to reach the critical energy density, of about $\varepsilon \approx 2.5$ GeV/fm^3, at which the deconfinement transition is predicted to

occur.

The Bjorken approach toward an estimate of ε can not be applied at an energy of 60 GeV/nucleon or below. Neither is the condition of a flat rapidity distribution (boost invariance) fulfilled here, nor should one employ the standard estimate for the formation time. We thus did not investigate the dependence of ε on the incident energy.

A separate analysis of electromagnetic and hadronic E_T values shows no excursions in their event by event ratio, away from the statistical fluctuations. Thus at our level of statistics we see no 'Centauro'–type events. The average value of E_T^{EM}/E_T^{HAD} is about 0.40 in central collisions, somewhat lower than the Fritiof value of about 0.45, characteristic of p+p collisions. This could be caused by a change in the final state hadron population, e.g. an enhancement of heavier hadrons. Although in agreement with recent observations, this conclusion can not be unambiguously reached in our investigation because of a systematic uncertainty in the separation of E_T^{EM} and E_T^{HAD}, of similar magnitude as the effect we observe.

In looking forward to experiments with lead beams at the CERN SPS, we expect the average energy density of average central collisions not to increase much further than to $\varepsilon \approx 2.6$ GeV/fm^3. Furthermore, the fall–off in the differential E_T spectra, toward the tail region, should be very steep. Events with a significantly higher E_T than that of 'central' collisions will thus be very rare. However, the energy density in the interior sections of the interaction volume, say within a radius of ^{32}S–dimensions (3.8 fm), might increase beyond 3 GeV/fm^3 [24]. Thus, the necessary preconditions (large volume, $\varepsilon \geq 2.5$ GeV/fm^3) of quark–gluon plasma formation should be met with lead beams.

Acknowledgement

We wish to thank the CERN accelerator and experimental area groups for providing excellent working conditions. This work was supported by the Bundesministerium für Forschung und Technologie, Germany, by the US departement of Energy (Contracts DE-AC03-76SF00098 and DE-AC02-76CH00016), the Hellenic Secretariat for Research and Technology and the Commision of the European Communities in cooperation with the Ministry for Science of Croatia.

References

[1] Proc. Quark Matter 1987, Z. Phys. **C38** (1988);
Proc. Quark Matter 1988, Nucl. Phys **A498** (1989);
H. Satz: Nucl. Phys. **A488** (1988) 511;
L. McLerran: Rev. Mod. Phys. **58**

[2] NA35 Collab., A. Bamberger et al.: Phys. Lett. **B184** (1987) 271

[3] A. Franz: Ph.D. Thesis, Univ. Siegen 1986

[4] NA35 Collab., J. Bächler et al.: Preprint GSI-90-69;
S. Wenig: Ph.D. Thesis, Univ. Frankfurt 1990 and
NA35 publication in preparation

[5] B. Andersson et al.: Phys. Reports **97** (1983) 31;
Nucl. Phys. **A498** (1989) 93; Nucl. Phys. **B281** (1987) 289;
B. Nilsson-Almqvist and E. Stenlund: LU-TP-86-14;
Comp. Phys. Comm. **43** (1987) 387;
T. Sjöstrand: Comp. Phys. Comm. **39** (1986) 347;
LU-TP-82-3; LU-TP-85-10; LU-TP-86-22

[6] NA35 Collab., A. Sandoval et al.: Nucl. Phys. **A461** (1987) 465

[7] C. de Marzo et al.: Nucl. Instrum. Methods. **217** (1983) 405;
Phys. Rev. **D29** (1983) 405;
M. de Palma et al.: Nucl. Instrum. Methods. **216** (1983) 393;
V. Eckardt et al.: Nucl. Instrum. Methods **155** (1978) 389;
J. Fent et al.: Nucl. Instrum. Methods **211** (1983) 315

[8] V. Artemiev et al.: Nucl. Instrum. Methods **224** (1984) 408;
M. Fuchs: Ph.D. Thesis, Univ. Freiburg 1985;
C. de Marzo et al.: Phys. Rev. **D36** (1987) 8 (and 16);
R. Marx: Ph.D. Thesis, Univ. Freiburg 1987;
M. Wülker: Ph.D. Thesis, Univ. Freiburg 1987;
C. Loos: Dipl. Thesis, Univ. Freiburg 1987;

F. Zetsche: Dipl. Thesis, Univ. Freiburg 1987;
E. Skodzek: Ph.D. Thesis, Univ. Freiburg 1988

[9] C.W. Fabjan: Preprint CERN-EP/85-54

[10] S. Margetis: Ph.D. Thesis, Univ. Frankfurt 1990

[11] NA35 Collab., W. Heck et al.: Z. Phys. **C38** (1988) 19

[12] NA35 Collab., A. Bamberger et al.: Phys. Lett. **B205** (1988) 583;

[13] R. Yoshida et al.: Phys. Rev. **D35** (1987) 388;
J. Cleymans et al.: Phys. Rev. **D35** (1987) 388;
A.D. Panagiotou et al.: Z. Phys. **A333** (1989) 355

[14] NA35 Collab., J. Bartke et al.: Z. Phys. **C48** (1990) 191;

[15] NA38 Collab., M. C. Abreu et al.: Preprint LAPP-EXP-89-15

[16] NA34 Collab., T. Akesson et al.: Z. Phys. **C38** (1988) 383;
Phys. Lett. **B214** (1988) 295; CERN-PPE/90-130

[17] WA80 Collab., R. Albrecht et al.: Phys. Lett. **B199** (1987) 297

[18] E802 Collab., T. Abbott et al.: Phys. Lett. **B197** (1987) 285;
Z. Phys. **C38** (1988) 383

[19] H. Satz: Annu. Rev. Nucl. Part. Sci. **35** (1985) 245;
F. Karsch: Z. Phys. **C38** (1988) 147

[20] J.D. Bjorken: Phys. Rev. **D27** (1983) 140;
L. McLerran: Proc. Quark Matter 1984 (Springer, Berlin, 1985) 1

[21] K. Werner and M. Kutschera: Phys. Lett. **B183** (1987) 385;
K. Werner: BNL preprint 39726; Phys. Lett. **B208** (1988) 520;
Lecture Notes, BNL 1988; CERN-TH-5682/90;
CERN-TH-5701/90; CERN-TH-5831/90

[22] T. Csörgö et al.: Preprint KFKI-1989-56/A;
Phys. Lett. **B222** (1989) 115

[23] A. Bialas, M. Bleszynski, W. Czyz: Nucl. Phys. **B111** (1976) 461

[24] R. Stock: Nucl. Phys. **A498** (1989) 333;
G.W. London, N.A. McCubbin and R. Stock: CERN report SPSC 87-52